POLITECNICO
MILANO 1863

SCUOLA DI INGEGNERIA INDUSTRIALE
E DELL'INFORMAZIONE

Wheel-rail interaction models for rail corrugation monitoring through axlebox acceleration measurements

Tesi di Laurea Magistrale in
Mechanical Engineering - Ingegneria Meccanica

Author: **Laurens Lanzillo**

Student ID: 969119
Advisor: Prof. Egidio Di Gialleonardo
Co-advisors: Ing. Leonardo Faccini, Ing. Claudio Somaschini
Academic Year: 2021-22

Abstract

Rail corrugation is a degradation phenomenon that affects most of railway lines. It consists of a quasi-periodic irregularity on the railhead which interacts with the wheels passing over it, causing high dynamic forces which, in turn, may damage the vehicle or the tracks and cause discomfort and vibrations. No definite solutions exist for all types of corrugation: the most frequently used treatment is periodic rail grinding. Costs associated with these maintenance operations and the need to optimize them make rail corrugation monitoring a priority for infrastructure managers.

In this thesis, an algorithm for the identification and monitoring of rail corrugation growth using axlebox acceleration measurements taken from an instrumented trainset is developed, starting from a state-of-the-art approach to the problem. Different models for the analysis of wheel-rail interaction in the frequency domain are derived to compute the measurement system transfer function. At first, the vertical dynamics of the interaction between wheel and rail is investigated. Effects of the full dynamic of the wheelset and the influence of the inclination of the wheel-rail contact plane are then added. The transfer functions obtained by these models are used for the estimation of railhead irregularity profile from axlebox acceleration measurements.

The robustness of this approach is investigated, discovering that changes in the measurement system parameters and speed variations cause a large dispersion of the results. This is particularly evident when the system is excited at frequencies corresponding to resonances in the wheel-rail dynamics. The possibility of monitoring the evolution of corrugation over time with the use of subsequent surveys is verified.

Keywords: Axle-Box Acceleration, Rail Roughness, Corrugation monitoring, Wheel-rail interaction

Abstract in lingua italiana

La marezzatura delle rotaie è un fenomeno di degrado dell'infrastruttura che interessa quasi tutte le linee ferroviarie. Essa consta in un'irregolarità quasi-periodica presente sulla superficie superiore delle rotaie che interagisce con le ruote che vi passano sopra, provocando quindi lo scambio di elevati carichi dinamici che, a loro volta, possono danneggiare il veicolo o i binari e causare disagi e vibrazioni. Non esistono soluzioni definitive per tutti i tipi di marezzatura: il trattamento più utilizzato contro di esse è la molatura periodica delle rotaie. I costi associati a queste operazioni di manutenzione e la necessità di ottimizzarle rendono il monitoraggio delle rotaie una priorità per il gestore dell'infrastruttura.

In questa tesi viene sviluppato un algoritmo per l'identificazione e il monitoraggio della crescita della marezzatura utilizzando le misure di accelerazione in boccola acquisite da un convoglio strumentato, partendo dallo stato dell'arte. La funzione di trasferimento del sistema di misura viene ricavata tramite lo sviluppo di diversi modelli per l'analisi dell'interazione ruota-rotaia nel dominio delle frequenze. In un primo momento, viene analizzata la dinamica verticale dell'interazione tra ruota e rotaia. Gli effetti della dinamica completa della sala e l'influenza dell'inclinazione del piano di contatto ruota-rotaia vengono quindi aggiunti. Le funzioni di trasferimento ottenute da questi modelli sono quindi utilizzati per stimare il profilo di irregolarità della rotaia a partire da misure di accelerazione.

La robustezza di questo approccio viene quindi analizzata, scoprendo che le variazioni dei parametri del sistema di misura e le variazioni di velocità causano una grande dispersione dei risultati. Ciò è particolarmente evidente quando il sistema di misura viene eccitato a frequenze corrispondenti a risonanze del sistema ruota-rotaia. Si verifica la possibilità di monitorare l'evoluzione della marezzatua nel tempo mediante l'uso di misurazioni successive.

Parole chiave: Accelerazione in Boccola, Rugosità, Monitoraggio della Marezzatura, Interazione ruota-rotaia

Contents

Introduction

Proper maintenance has always been a fundamental priority for any major railway network to obtain a safe and efficient passenger and freight service. Moreover, maintenance plays a key role in ensuring regularity during operations. Therefore, over the years railway companies have developed specific maintenance practices to address their track quality standards.

Different kinds of maintenance operations can be carried out on railway lines, usually following a schedule depending on the expected track load cycles [1]. Such processes are normally performed by specialized machines which cannot execute their task alongside normal traffic. Therefore, particular care must be taken by the railway operators to plan rail maintenance operations, optimizing the timing and location of working areas to avoid an expensive logistical burden. This need, combined with the non-uniform wear rate of track lines along their extension, calls for the need of acquiring reliable data about the health state of railway infrastructure to properly prioritize maintenance sites. Traditionally, this has been done with approaches based on a fixed schedule, empirical evidence of degraded sections, as well as inspections along the lines, carried out with purpose-built vehicles while normal operations are interrupted. Such equipment is usually acquired or rented by railway operators in small numbers and is limited to speeds of a few kilometers per hour: having to cover large networks, they result in large lapses between two consecutive passages on a specific section.

Luckily, this issue can be addressed by technology: the development of inexpensive accelerometers and other measurement systems allows railway operators to install them on the very vehicles they run on their networks, transforming their entire fleets (or large parts of them) into frequent and continuous diagnostic vehicles. These measurement systems can be composed of a series of accelerometers mounted on the vehicle plus a data storage system and some auxiliary subsystems (interfaces with trainset odometers and speedometers,...) [2]. The information which can be acquired by such systems is an indirect measurement: further processing is therefore required if the objective is to obtain a reconstruction of the irregularity profile. However, such systems can detect a wide variety of track defects [3, 4] as well as malfunctions and faults at train-level [5]. Their continuous

and daily rail network coverage allows operators to closely follow and monitor degradation levels over time and put sophisticated *condition-based maintenance* practices into service.

Within this vast framework, this thesis focuses on using accelerometer-equipped axleboxes to identify a specific degradation phenomenon called *rail corrugation*. This phenomenon is present in most of the railway networks and consists of a quasi-periodic irregularity of the rail running surface: these periodic irregularities can give rise to high dynamic loads between wheel and rail [6]. These loads can, in turn, produce degradation of railway components as well as annoying vibration and sound emissions in the audible frequency range. Corrugation growth can be arrested by removing the irregularity by reprofiling the rail running surface. This is accomplished through rail grinding: identifying corrugation at the early development stage is therefore of paramount importance for railway operators to properly schedule the aforementioned maintenance practices.

Corrugation detection systems can either rely on direct analysis of the acceleration signal [7] or obtain a reconstruction of the rail profile through the Transfer Function of the measurement system [8]. From this profile, some synthetic indexes can be obtained: if they overcome a predefined threshold, then rail grinding operations can be scheduled to restore the original track profile [9].

This thesis aims to follow this latter approach, by developing an algorithm for the identification of rail corrugation starting from acceleration data acquired in the subway system of Milan. The rail profile is estimated from acceleration measurement using a frequency domain model of wheel-rail interaction developed from the work exposed in [10] and [11]. The algorithm is then validated using both tests on its robustness as well as data coming from corrugation measurements made on-site by a specialized diagnostic railcar and kindly provided by Milan Transit company ATM.

This thesis is divided into five chapters, organized as follows:

- **First chapter** presents a detailed overview of rail corrugation. Different types of corrugation and their root causes are presented, and the principal options for rail corrugation treatment are discussed. Moreover, an analysis of the principal methodologies of corrugation detection is performed. The most common measurement systems currently in use are compared, and their strengths and weaknesses are discussed. Finally, some common treatments against different types of corrugation are exposed.
- **Second chapter** details the layout of an axlebox accelerometers-based measurement system. The interaction models between the wheelset and rails are discussed.

From them, the measurement system transfer functions are derived. Several cases with greater complexity are presented, starting from a simple system that neglects wheel coupling to more complex and refined multi-input - multi-output models. Then, the theory behind the experimental modal analysis of the wheelset is presented. A brief explanation of the method for computing track receptances is finally exposed, alongside its experimental validation.

- **Third chapter** presents the experimental modal analysis carried out during the thesis alongside its results. The results of the experimental activity are used to validate and adjust a modal model of the wheelset obtained via a Finite Element Analysis. From the latter, wheelset receptances are computed.
- **Fourth chapter** exposes the results of the axlebox accelerometers-based measurement system. Its robustness is investigated using data from a line section of Milan's underground network. The algorithm is then used to monitor the evolution of corrugation over time.
- Some conclusions regarding the work of this thesis are finally exposed in the last chapter.

1 | State of the Art

In this chapter, rail corrugation is presented: different embodiments of the phenomenon are analyzed and classified, according to their typical frequency, damage, and wavelength-fixing mechanisms. Several methods of corrugation detection are also introduced and compared. Some common treatments currently employed against different types of corrugation are exposed. Finally, a brief description of the methods used to investigate corrugation growth is given, as well as an overview of the main methodologies of corrugation growth modeling.

1.1. Rail corrugation classification

The term Rail corrugation encompasses a range of phenomena with different manifestations and root causes that share a common formation scheme, as presented by Grassie in [6] and illustrated in Figure 1.1.

This formation mechanism is based on a feedback loop: an initial rail profile - having a casual distribution of irregularities - interacts with the rolling stock passing over it. The induced vibrations of the wheelset cause the exchange of forces between them and the track, which in turn excites a so-called *wavelength-fixing mechanism*, i.e. the dynamics of the wheel-rail interaction, the dynamic behavior of wheel and rail. Wavelength-fixing mechanisms determine the most likely corrugation wavelength and position along the tracks. Other parameters, such as wheel-rail friction, and track geometry, etc... can influence this dynamic mechanism. Moreover, these forces act as the main driver of the *damage mechanism*, typically *plastic flow* or *wear*. Damage mechanisms modify the initial rail profiles: damaged rails further interact with subsequent passages of trains, thus accentuating the phenomenon. An example of a rail affected by corrugation can be appreciated in Figure 1.2. The two circles highlight two different corrugation wavelengths.

Figure 1.2: Track affected by corrugation.

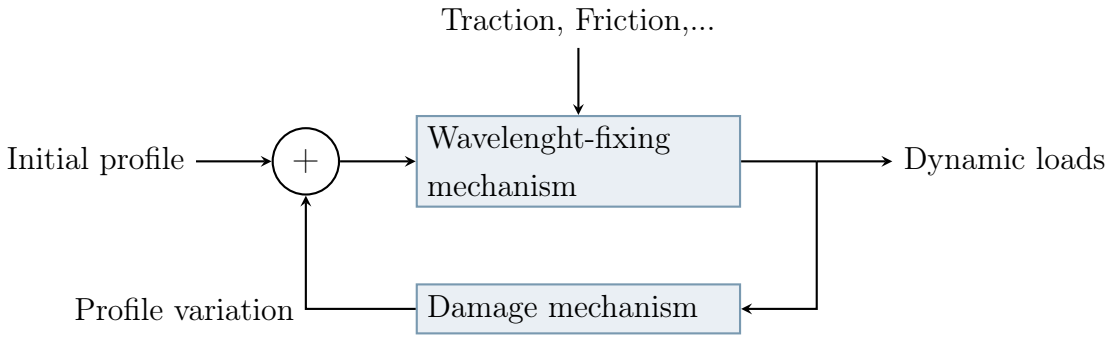

Figure 1.1: General corrugation mechanism (as exposed in [6]).

Being railway engineering a mature research field, over the past decades the most common types of corrugation have been studied and classified. Table 1.1 summarises them. Although the frequency f at which the wavelength-fixing mechanism operates is fixed and dependant on its dynamics [6], the spatial wavelength λ at which corrugation appears depends on rolling stock speed v, with the relation (1.1) bonding them.

$$\lambda = \frac{v}{f} \tag{1.1}$$

Transit networks are often affected by more severe corrugation with respect to mixed-traffic lines, since the former tend to have a limited number of train types that operate at high frequencies and homogeneous velocities. Any wavelength-fixing mechanism which results in corrugation is therefore consistently excited, resulting in a faster corrugation growth with respect to mixed-traffic lines. The following sections contain an overview of the main types of corrugations.

Type	Wavelenght-fixing mechanism	Typical frequency (Hz)	Damage mechanism
Pinned-pinned resonance ('roaring rails')	Pinned-pinned resonance	400-1200	Wear
Rutting	Second torsional resonance of driven axle	250-400	Wear
Heavy haul	P2 resonance	50-100	Plastic flow in troughs
Light rail	P2 resonance	50-100	Plastic bending
Other P2 resonance	P2 resonance	50-100	Wear
Trackform-specific	Trackform specific	-	Wear

Table 1.1: Types of corrugation and their characteristics (according to [12])

1.1.1. Pinned-Pinned resonance or 'roaring rails' corrugation

This type of corrugation occurs mainly in straight track sections or high-radius curves, in the latter case primarily in the high rail. This corrugation is caused by the resonance of the rail, acting almost like a beam pinned at the sleepers. It is possible to compute this frequency with Equation (1.2):

$$f = \frac{\pi}{2L_s^2}\sqrt{\frac{E_r I_r}{m_r}}\left[1 - \frac{1}{2}\left(\frac{\pi r_g}{L_s}\right)^2\left(1 + \frac{2(1+\nu_r)}{\kappa_r}\right)\right] \tag{1.2}$$

where E_r is the rail Young's modulus, I_r its 2nd moment of area, m_r its mass, L_s the supports spacing, ν_r rail Poisson modulus, r_g its gyration radius, and κ_r the shear factor of the cross-section.

A typical resonant frequency is about 770 Hz for a 56 Kg/m rail and a 0.7 m support spacing or around 1200 Hz for a 60 Kg/m rail and 0.6 m spacing [12]. Corrugation is worse over sleepers due to higher rail vertical stiffness. The damage mechanism for this type of corrugation is wear: the high dynamic forces exchanged between the railhead and the rolling stock (a 0.1 mm irregularity may be sufficient to cause contact loss in the

corrugation troughs and therefore a continuous 'hammering' of the wheel along the track) encourage slip and wear of the thoughs.

1.1.2. Rutting corrugation

Rutting corrugation is a corrugation characterized by a frequency of around 250-400 Hz, caused by the second torsional resonance of driven wheelsets. Rutting commonly occurs when the traction ratio on one wheel is close to the friction limit, generating wheel slip. Sudden loss of adhesion causes the opposite wheel of the wheelset to start a stick-slip oscillation. Such a phenomenon usually happens in the high rail of the leading wheelset in a bogie during a curve, due to the higher tangential force and the lower friction coefficient (also due to contaminants coming from flange lubricators which migrate from the gauge face of the high rail). The damage mechanism is wear. Since the friction coefficients strongly affect the slip phase of the roll-slip oscillation, intervening on them can be an effective way of reducing rutting corrugation.

1.1.3. Heavy haul corrugation

Heavy haul corrugation usually identifies the type of corrugation found in railways characterized by large axial loads, typically freight lines. This type of corrugation is nowadays widely understood and mostly solved. It is caused by the excitation of P2 resonance, i.e. the vertical oscillation of the wheelset and rail. This resonance occurs at a frequency defined by Equation (1.3)

$$f = \frac{1}{2\pi}\sqrt{\frac{K_{track}}{m_{track} + m_{wheelset}}} \tag{1.3}$$

where K_{track} is the equivalent stiffness of the track and m_{track} and $m_{wheelset}$ are the equivalent masses of the corresponding components. This excitation, if exited by defects such as welds or rail joints, acts as the wavelength-fixing mechanism. Damage to the railhead is in turn caused by plastic flow of metal, a mechanism exacerbated by the heavy axial load in the rail sections under analysis, as well as the presence of cant excess for some of the rolling stock in mixed-traffic railway lines.

1.1.4. Light rail corrugation

Light rail corrugation is also caused by P2 resonance. In this case, the damage mechanism is not plastic flow but rather rail plastic bending. This problem has successfully been solved by employing materials and rail sections with greater yield strength and a reduced number of initial defects (welds or joints) to reduce the possible starting points

of corrugation.

1.1.5. Other P2 resonance corrugation

In some cases, where P2 resonance has a frequency comparable to the first torsional resonance of wheelsets, severe corrugation can arise. This type of corrugation can cause a low-frequency 'rumble' to be transmitted to the surrounding buildings and structures. In this case, the damage mechanism is usually wear. This type of corrugation is present in several metro and tram systems, especially when high-stiffness rail supports are used.

1.1.6. Trackform-specific corrugation

Trackform-specific corrugation is usually related to severe resonance in the track structure. The lightly damped resonance of a large baseplate can act as the wavelength-fixing mechanism. Some trackforms, such as sleepers mounted in resilient boots, are particularly prone to corrugation on the lower rail of curves.

1.2. Irregularity measurement techniques

To measure rail irregularity, several measurement systems have been developed. These systems were developed to properly prioritize rail grinding operations along networks due to their costs and impacts on train circulation, since grinding the whole network at fixed, regular intervals is neither an efficient nor a cheap option for rail operators. By properly detecting corrugation at an early stage, grinding operations can be scheduled in order not to disrupt normal operations and at the same time save railheads from severe consumption due to wear or excessive grinding. Grassie offers an overview of the three most diffused methods in [8]:

- Chord-based measurement systems;
- Low-speed accelerometer-based systems
- Axlebox accelerometer systems

Each of them has its characteristics, pros, and cons, summarized in Table 1.2. Their performances are analyzed mathematically by computing their transfer functions and highlighting their operational benefits in the following sections.

Measurement system type	Pros	Cons
Chord-based measurement systems	Cheap, independent from speed or vibration	Highly nonlinear, therefore it needs some information regarding the expected wavelength(s)
Low-speed accelerometer-based systems	Accurate below resonance speed	Delicate, low measurement speed, sensible to vehicle and track vibrations
Axlebox accelerometer systems	Cheap, robust, easily scalable to a whole train fleet	Wheel and track dynamics must be taken into account

Table 1.2: Advantages and disadvantages of different measurement systems.

1.2.1. Chord-based measurement systems

Chord-based measurement systems were the first to be developed. They are based on a horizontal bar having length L, supported at both ends on the rail. From this bar, measurements are taken by vertical probes (probes can either be mechanical or laser transducers). These probes are set at a distance α from one bar extremity. Figure 1.3 shows the layout of such a system. When analysing a sinusoidal irregularity with ampitude

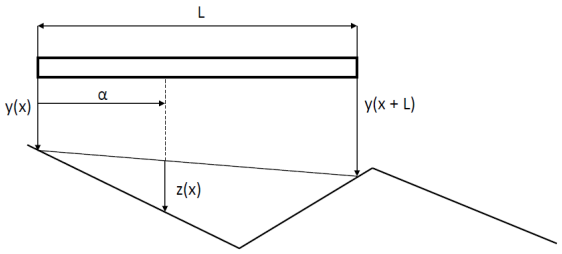

Figure 1.3: Layout of a chord-based corrugation measurement system.

Y and wavelength λ such as:

$$y(x) = Y \sin\left(\frac{2\pi x}{\lambda}\right) = Y \sin(kx) \tag{1.4}$$

where $k = 2\pi/\lambda$ is the *wavenumber*. It is possible to compute the system's measurement on the point z as:

$$\begin{aligned} z(x) &= y(x + \alpha L) - \{y(x) - \alpha[y(x + L) - y(x)]\} \\ &= Y \sin(kx)[\cos(\alpha x L) - \alpha \cos(kL) - (1 - \alpha)] \\ &+ Y \cos(kx)[\sin(\alpha x L) - \alpha \sin(kL)] \end{aligned} \tag{1.5}$$

From this equation and by rearranging amplitude Z and phase Φ as functions of the wavenumber and the instrument geometry defined by the λ/L ratio:

$$\begin{aligned} Z &= Y\{[\cos(\alpha x L) - \alpha \cos(kL) - (1 - \alpha)]^2 + [\sin(\alpha k L) - \alpha \cos(kL) - (1 - \alpha)]^2\}^{1/2} \\ \Phi &= \tan^{-1}\left[\frac{\sin(\alpha k L) - \alpha \cos(kL)}{\cos(\alpha k L) - \alpha \cos(kL) - (1 - \alpha)}\right] \end{aligned} \tag{1.6}$$

Figure 1.4 shows the Magnitude of the transfer function Z/Y shown in Equation (1.6) as a function of the ration λ/L for different α/L rations. The Transfer Function is highly nonlinear, with some wavelengths greatly amplified while others are drastically reduced. Installing more transducers on the same instrument can aid in solving this issue, broadening the peaks of the transfer function. Moreover, there is no speed influence on the Transfer Function. Moreover, such systems are not sensible to rail or vehicle vibrations [8]. Chord-based measurement systems have been used by [13] to measure railhead roughness. In their work, optical devices are used instead of probes to overcome the aforementioned speed limitations associated with chord-based measurement systems.

1.2.2. Low-speed accelerometer-based systems

Another possibility for measuring rail irregularity is the use of a low-speed accelerometer-based system. A transducer is placed on a rigid body having a mass m, which in turn makes contact with the rail through a pad that has a finite stiffness K and a hysteresis loss factor η. A representation of the layout can be appreciated in Figure 1.5. If a sinusoidal irregularity of amplitude Y and wavelength λ as represented in:

$$y(x) = Y \sin\left(\frac{2\pi x}{\lambda}\right) \tag{1.7}$$

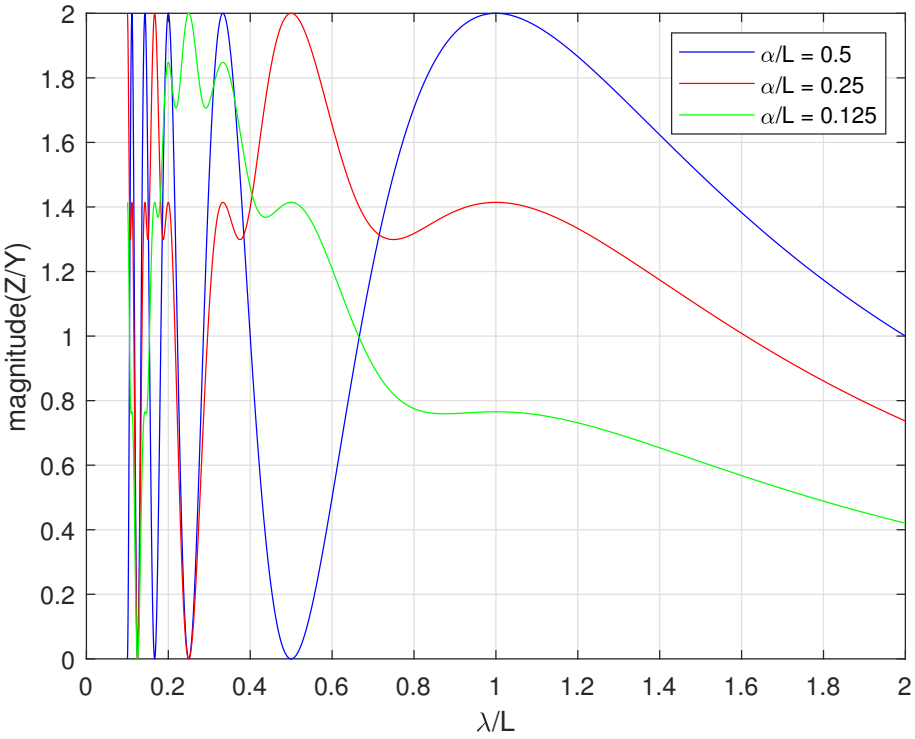

Figure 1.4: Transfer function of a chord-based corrugation measurement system

where $x = vt$ is the position of the rail with respect to time and v is the speed of the measurement system. By substituting $\Omega = 2\pi v/\lambda$ it is possible to rewrite irregularity as:

$$y(t) = Y \sin \Omega t \tag{1.8}$$

It is now possible to compute the equation of motion of the rigid body to which the accelerometer is attached in the vertical direction by writing:

$$m\ddot{z} = k(1 + j\eta)(y - z) \tag{1.9}$$

This is a second-order differential equation having infinite solutions. By knowing the sinusoidal shape of the input, it is possible to impose a rigid body displacement in the form $z(t) = Zsin(\Omega t)$. The displacement ratio Z/Y is therefore given by:

$$\frac{Z}{Y} = \frac{k(1 + j\eta)}{-m\Omega^2 + k(1 + j\eta)} \tag{1.10}$$

the system posesses a natural frequency Ω_0, given by:

$$\Omega_0 = \sqrt{\frac{k}{m}} \tag{1.11}$$

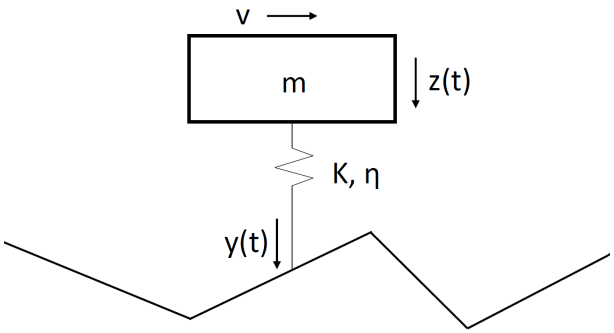

Figure 1.5: Layout of a low-speed accelerometer-based measuring system.

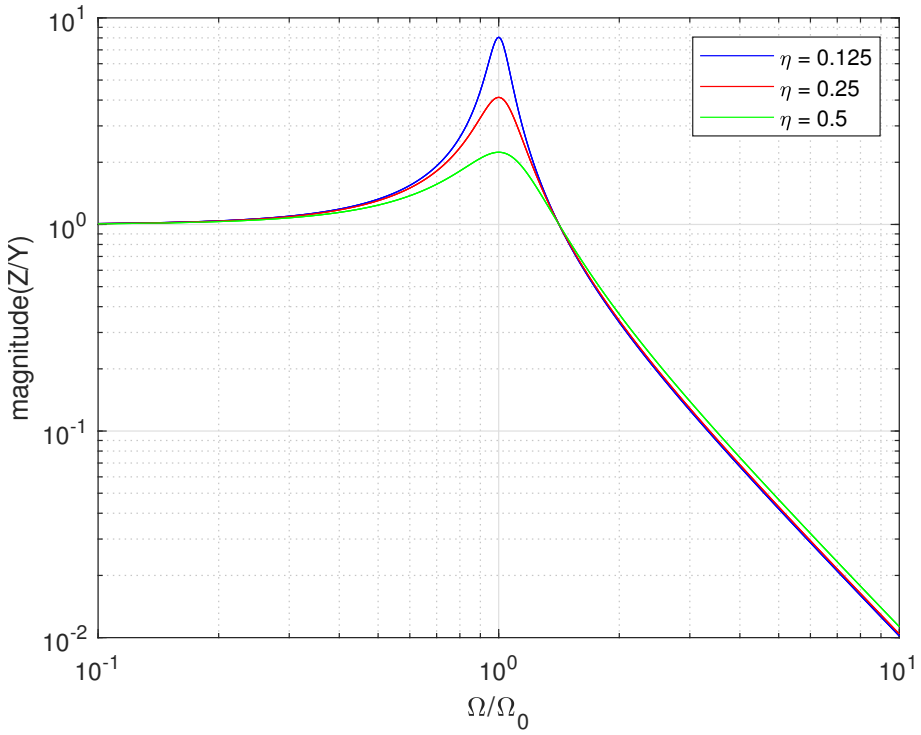

Figure 1.6: Transfer function of a low-speed accelerometer-based measuring system.

It is possible to plot the obtained system response as a function of the *adimensional frequency* $f/f_0 = \Omega/\Omega_0$ for different values of the loss factor η. The results are highlighted in Figure 1.6.

It is possible to appreciate that, below Ω_0, the measurement system can reproduce correctly the behavior of rail irregularities. Therefore, for the system to work correctly, it must be moved far below its critical speed $v_0 = 2\pi\lambda_{min}/\Omega_0$, where λ_{min} is the minimum length of the irregularity to be detected. This can make such a layout impractical when surveying long line sections. Moreover, these systems are also sensitive to both vehicle

and rail vibration, and properly insulating them can be challenging.

1.2.3. Axlebox accelerometer systems

Limitations of low-speed accelerometer measuring systems can partially be overcome by axlebox accelerometer-based systems. Thanks to their simplicity and robustness, these systems are probably the most common instruments to measure rail irregularity at service speed. These systems are based on measurements coming from accelerometers attached to the axleboxes of railway axles, which can either be modeled as rigid bodies or by introducing compliances. This acceleration can be linked to the rail contact force using the wheel and rail receptances, as well as appropriate modeling of contact between rail and wheel. There are different modeling strategies to compute the transfer function of

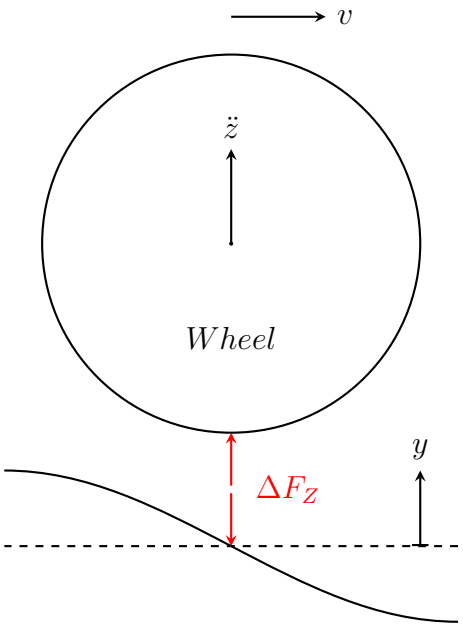

Figure 1.7: Layout of a simple axlebox accelerometer measurement system.

such a system, with a simple layout being presented in Figure 1.7. As previously done, it is possible to start from a sinusoidal irregularity defined as $y(t) = Ye^{j\Omega t}$. The dynamic contact force exchanged between the wheel and the railhead can also be described as a sinusoidal function of time $\Delta f(t) = \Delta F e^{j\Omega t}$, with ΔF being a complex quantity. These two quantities are bonded by Equation (1.12):

$$\frac{\Delta F}{Y} = \frac{1}{A_w + A_r + \frac{1}{K_H}} \tag{1.12}$$

where K_H is the linearised Hertzian stiffness, A_w and A_r are the wheel and rail receptances. While, in some simple approximations, the wheel is treated as a rigid body, due to the measurements being taken at service speed, it is often necessary to take into account wheel and rail flexibility. An example of this can be traced in the work of Tassilly [14] and Grassie [8]. It is then possible to link contact force and the vertical acceleration detected in the axlebox via the receptance between the wheel's contact point and the accelerometer placed in the axlebox $\ddot{Z} = -\Omega^2 A_b \Delta F$, where $\ddot{Z}$ is the measured acceleration. The transfer function between the measured acceleration and rail profile is therefore described by (1.13).

$$\frac{Y}{\ddot{Z}} = -\frac{A_w + A_r + \frac{1}{K_H}}{\Omega^2 A_b} \tag{1.13}$$

Axlebox acceleration systems have the advantages of permitting monitoring at commercial train speed as well as their lower cost compared to more sophisticated systems. However, due to the high forces and loads, train and track dynamics interact with each other. Therefore none of them can be neglected in the measurement system transfer function. Moreover, Equation (1.13) shows how the dynamic characteristics of the rail constitute part of the transfer function. Therefore, some parameters regarding its modeling must be known in advance. These parameters can widely change along the line, being therefore a potential inaccuracy source. However, for practical purposes a statistical representation of the rail profile is sufficient: several acquisitions can be averaged to obtain it. This is commonly accomplished by computing the roughness variance over a defined wavelength window over a defined section of track. The evolution of this measurement over time can therefore be used to monitor track health.

An axlebox acceleration measurement system was used by [15] for the estimation of longitudinal profile irregularities in the range of 10-3000mm. An implementation of an irregularity measurement system based on axlebox accelerometers will be the core of this thesis.

It is worth noticing that [16] has demonstrated the possibility of using a *combined approach* using a combination of different approaches. First, a one-dimensional convolution neural network to identify and classify rail corrugation based on data coming from the accelerometers. A vehicle–track coupling dynamics model to estimate the dynamic response of the axlebox. Finally, a surrogate model is used to compute corrugation depth. This combined approach is able to both identify corrugation and correctly estimate its depth. This approach works successfully even when varying the track substructure, a common limit for *axlebox accelerometer systems* [8].

1.3. Corrugation treatment

Several treatments have been proven efficient in corrugation treatment.

One of the most commonly used treatments for corrugation is *reprofiling* or *rail grinding*, i.e. the restoration of the initial profile of the rails. This practice can prevent the recurrence of corrugation if the damage mechanism is excited by railhead defects (such in the case of *heavy haul* and *light rail* corrugation. However, if the damage mechanism is related to wear, rail grinding is only able to slow down the recurrence of corrugation [12]. Moreover, rail grinding can itself act like a wavelength-fixing mechanism if the grinding signature has any periodic behavior.

Hard rails slow down the development of all types of corrugation since they resist plastic flow and their high bending strength works against light rail corrugation. Moreover, they can alleviate any corrugation for which wear is the damage mechanism.

Another possible treatment against corrugation is *friction control*. A friction coefficient low enough to reduce wear but high enough to permit traction and braking can reduce damage from plastic flow and wear. This is usually accomplished by normal atmospheric humidity, moisture, and contaminants (leaves, rust,..). Excessive friction can become a problem in long, dry tunnels typical of subway systems.

Better curving wheelsets and a general reduction of tangential loads are often able to reduce the track's tendency of developing corrugation in curves. For the same reason, a reduction in cant is usually recommended in curves prone to corrugation. Moreover, wheelsets' resilience to torsional vibrations can help when dealing with corrugation arising from wheelset torsional resonances. It is also possible to act on the *trackform*, for example by reducing P2 resonance and increasing damping to counteract trackform-specific corrugation. However, it can be difficult to implement these measurements on a whole line.

1.4. Models for wheel-rail interaction

There are essentially two different approaches when modeling wheel-rail interaction: *time domain models* and *frequency domain models*. A brief description of their main features is given below.

1.4.1. Time domain models

In these models, the interaction between wheelset and rails is described as a system of equations that are solved numerically in the time domain. An example of this method can be found in the work of Nielsen [17], who investigated corrugation growth in the Dutch railway network. At first, an initial roughness profile is obtained in the form of a spectrum with wavelengths in a relevant range and random phases. Amplitudes are chosen so that the profile can approximate a smooth rail. The track is modeled as a series of Rayleight-Timoshenko beam elements, laying on uniformly-spaced sleepers. Sleepers are modeled as discrete masses, while rail pads and ballast are modeled as two layers of linear springs and viscous dampers. The train is modeled as a single rigid mass corresponding to one driven wheelset. Forces are estimated by numerically solving the interaction problem. Detailed computations can be found in [18]. Time domain models have also been used by [19] in the DB network and by [20] and [11] to investigate corrugation growth in the Milan subway network.

Time domain models have the distinct disadvantage of requiring high computational power. This requirement can be greatly reduced when choosing to use frequency-domain models, at the cost of simplifications in the choice of models, which must be linear. However, time domain models allow to properly model wheelset and rail non-linearities.

1.4.2. Frequency domain models

The frequency domain models' approach is based on the idea of considering rail irregularity as the only source of excitation of the system. Irregularity acts as a harmonic driving displacement, whereas the wheelset-rail interaction is either modeled as the results of a quasi-static, non-linear simulation linearized around a steady state condition or by means of an analytical interaction model. Examples of this approach can be found in the work of Frederick [21] and Tassilly [14]. The system's response to rail irregularity can then be computed separately for each frequency.

2 | Axlebox Accelerometer System Layout

In this chapter, the layout of the measurement system and the irregularity detection algorithms used in this thesis are explained. Different mathematical models used to investigate the wheel-rail interactions are exposed. The first model exposed is a single-input, single-output model oriented in the vertical direction which takes into account the dynamics of only half of the wheelset. Afterward, the cross effects of rail irregularity on both wheels are added, therefore obtaining a two-inputs, two-outputs model. Finally, the effect of lateral dynamics and the influence of the contact plane inclinations are added. The procedure to compute receptances of the wheelset under analysis is exposed and the theory behind a modal model validated experimentally is described. Finally, the receptances of the rail are derived from a mathematical model.

2.1. Measurement system layout

Data used for this thesis is acquired by a series of sensors placed in a trailer bogie of a *Meneghino* trainset operated by the transit company *Azienda Trasporti Milanesi* along the Milan underground network. One of the car's bogies is equipped with a series of 6 accelerometers, one measuring vertical acceleration for each axlebox plus one mounted laterally on one side of each wheelset. A detailed view of the sensors' position can be found in Figure 2.1, while Figure 2.2 depicts the accelerometers' placement on the axleboxes of the wheelset.

Depending on the travel direction, data coming from the three accelerometers in the bogie's leading wheelset is used. Accelerometers acquire data at a constant sampling frequency of 1000 Hz, while the trainset position is computed by integrating a velocity signal comping from an encoder, referenced through data of the Automatic Train Control system.

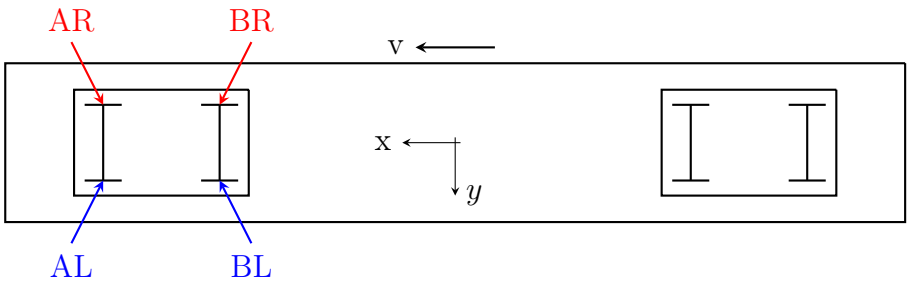

Figure 2.1: Instrumented car layout.

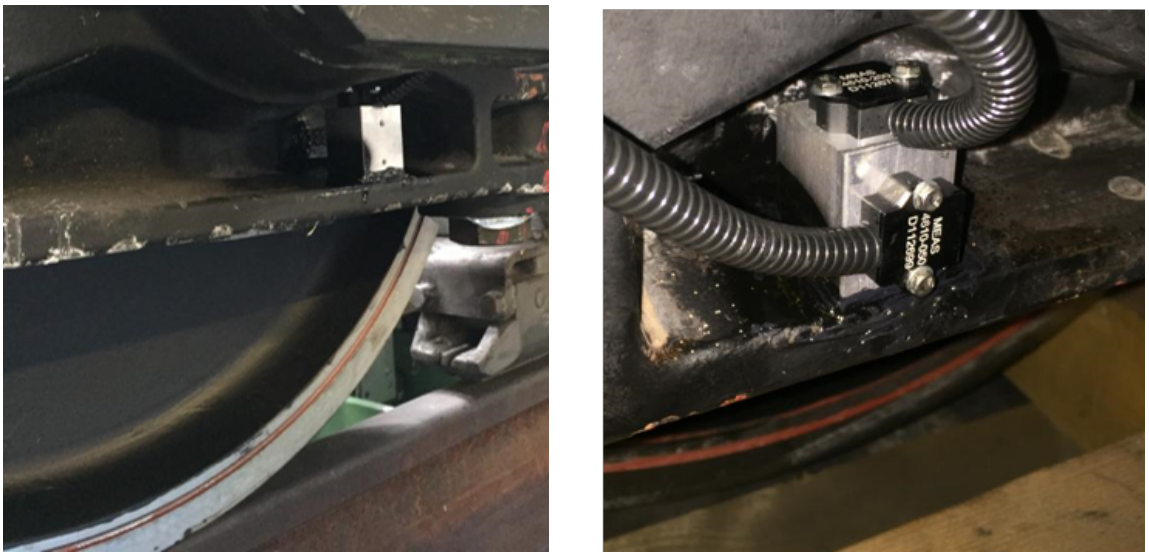

(a) Left side. (b) Right side.

Figure 2.2: Accelerometers mounted on the axleboxes.

2.2. Irregularity estimation algorithm

A detailed layout of the algorithms used in order to estimate rail corrugation can be appreciated in Figure 2.3. The detection algorithm aims at reconstructing the rail profile starting from the acquired acceleration measurements.

At first, data coming from the accelerometers is filtered and processed, obtaining a series of spectra. Acceleration spectra are then multiplied by the system transfer function to obtain irregularity spectra. From the irregularity spectra, several approaches are possible. While Grassie et al. described the possibility of extracting the RMS amplitude of railhead irregularity from the rail spectrum in [15], the approach used by Karaki et al. in [10] is followed in this thesis. An inverse Fourier transform is applied to the spectrum and the original rail profiles are reconstructed. From these, it is possible to directly compute the RMS amplitude of railhead irregularities on both rails. Since the computed irregularities

are a combination of both wheel and rail roughnesses, it is necessary to separate the two contributions. One possible approach has been followed by Carrigan et al. in [22], and it is based on the idea of exploiting the periodicity associated with the wheel roughness with respect to the random component present in rails. Acceleration samples are interpolated to obtain a fixed number of samples per wheel revolution. Signals are then filtered by means of a 4th-order zero-phase Butterworth notch comb filter, centered on the wheel rotational frequency.

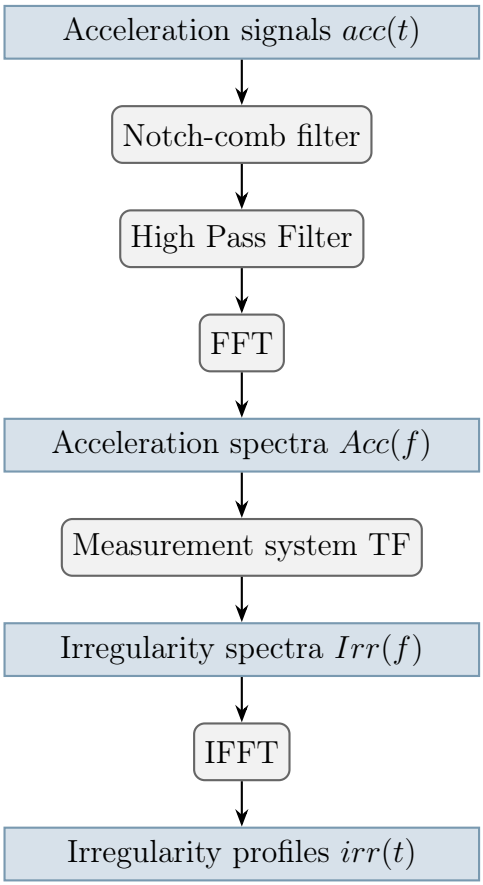

Figure 2.3: Irregularity detection algorithm layout.

To compute the transfer function of the measurement system, different approaches are tested:

- Considering only half of the wheelset, as done by [10];
- Considering vertical dynamic of the wheelset;
- Considering both vertical and lateral dynamics of the wheelset.

The procedure to obtain the receptances necessary to compute the transfer function of the measurement system will be exposed in the following sections. The contact between

the wheel and rail is treated within Hertz framework [23], allowing to approximate the force-displacement relation at the interface with a linear, Hertzian spring of stiffness K_H. All tangential forces are neglected, hence treating the problem as a pure normal contact one.

2.2.1. Half wheelset approach

In the case of the half wheelset layout, the two halves of the wheelset and the two rails are considered to be dynamically decoupled. The irregularities on each side will therefore only influence the accelerometer on the same side, neglecting each cross-component. The system's layout is represented in Figure 2.4. To obtain the transfer function linking vertical axleboz acceleration $\ddot{z}_A$ to the railhead irregularity z_R, it is possible to start from the displacement congruence at each wheel-rail interface:

$$z_{irr} = \Delta Z_W - \Delta Z_R + \Delta L_H \tag{2.1}$$

where z_{irr} is the railhead irregularity, ΔZ_W is the relative wheel vertical displacement, ΔZ_R is the relative rail vertical displacement and ΔL_H is the compression at the interface due to Hertzian contact and K_H is the Hertzian linearized stiffness. It is then possible to link these displacements to wheel and rail receptances:

$$\begin{aligned} \Delta Z_W &= A_{W,Z}(\Omega)\Delta F_Z \\ \Delta Z_R &= -A_{R,Z}(\Omega)\Delta F_Z \\ \Delta L_H &= K_H \Delta F_Z \end{aligned} \tag{2.2}$$

where $A_{W,Z}$ and $A_{R,Z}$ are the wheel and rail receptances in the contact point and along the vertical direction, while ΔF is the normal force exchanged at the contact point. The vertical force applied at the contact point can be linked to the axlebox displacement as:

$$Z_A = A_{Z,CP\to A}(\Omega)\Delta F_Z \tag{2.3}$$

by deriving twice the displacement it is possible to compute the acceleration in the Axlebox. Therefore, in the frequency domain, it is possible to write:

$$\ddot{Z}_A = -\Omega^2 A_{Z,CP\to A}(\Omega)\Delta F_Z \tag{2.4}$$

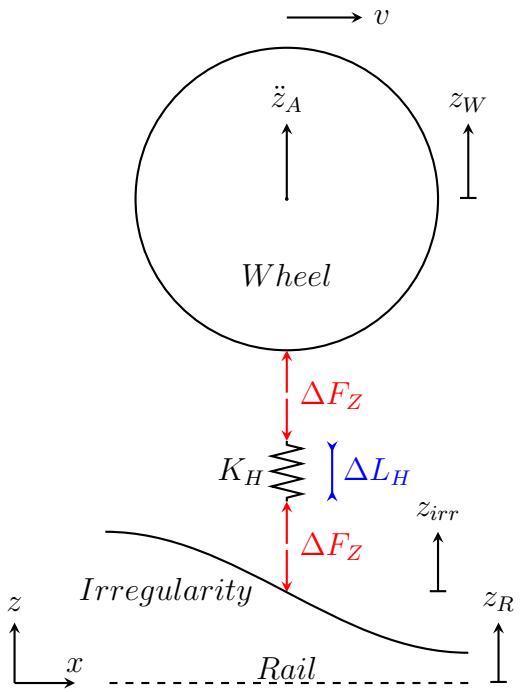

Figure 2.4: Single input design layout.

Finally, it is possible to write the complete relationship linking z_irr to the vertical force:

$$z_{irr} = (A_{W,Z} + A_{R,Z} + K_H)\Delta F_Z \tag{2.5}$$

and, by substituting the inverse of (2.4) into (2.5) the measurement system transfer function is obtained:

$$z_{irr} = \frac{A_{W,Z} + A_{R,Z} + K_H}{-\Omega^2 A_{Z,CP\to A}} \ddot{Z}_A \tag{2.6}$$

This transfer function allows for the computation of rail irregularity based on the acceleration data coming from the same side axlebox. This approach has been successfully adopted by Karaki et al. in [10] to develop a methodology to continuously monitor corrugation growth.

2.2.2. Vertical dynamic of the full wheelset

A more refined analysis can be performed by introducing cross terms between irregularity on the left side, measured acceleration on the right side and vice versa. This causes the model to effectively become a *two inputs, two outputs* system since now the full dynamic of the wheelset is accounted for. The two rails can still be considered dynamically decoupled. All the receptanes are referred to using the notation highlighted in Figure 2.5, i.e. $A_{6,3}$ denotes the receptance in direction 6 (left axlebox, z direction) due to input in direction

3 (left contact point, z direction).

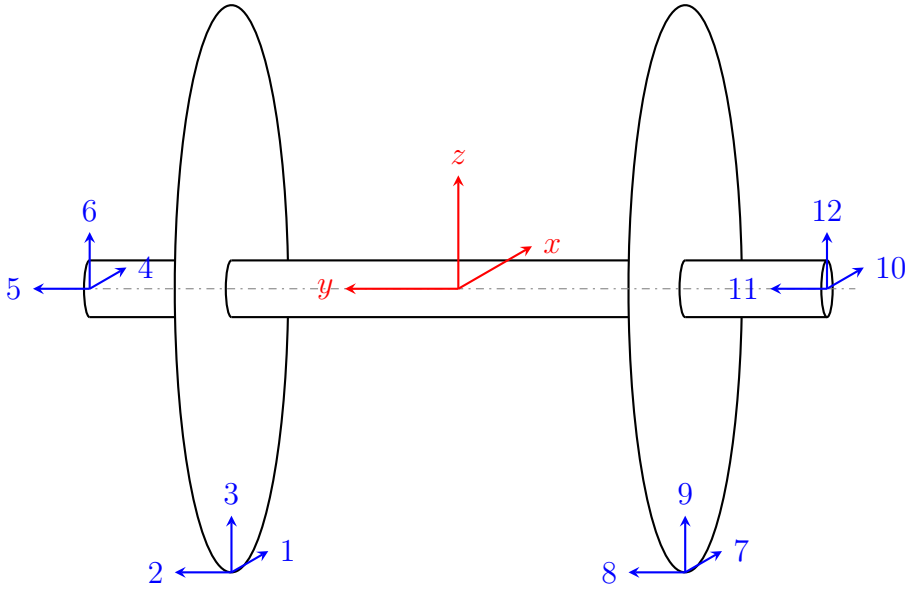

Figure 2.5: Receptances reference system.

Even if considering the full wheelset dynamics, the process is similar to a single wheel model: the irregularities on each track $z_{irr,L}$ and $z_{irr,R}$ are computed as a function of the relative displacements of wheel and rail, plus the contribution of each Hertzian contact spring. However, each wheel displacement must be linked to all the forces acting on the wheelset as represented in Figure 2.6, by means of the wheelset receptances.

At first, the irregularities on the two rails are written in the system of equations (2.7). For the sake of clarity, the first subscript indicates whether displacements are referred to Wheels, Rails, or Axlebox, while the second subscript identifies the side, either Left or Right.

$$\begin{cases} z_{irr,L} = \Delta z_{W,L} - \Delta z_{R,L} + \Delta L_{H,L} \\ z_{irr,R} = \Delta z_{W,R} - \Delta z_{R,R} + \Delta L_{H,R} \end{cases} \tag{2.7}$$

Given the fact that vertical displacements of the contact points happen on directions 3 and 6 within the reference framework 2.5 respectively, it is possible to rewrite displacements

using $\Delta F_{Z,L}$, $\Delta F_{Z,R}$ and the wheel receptances found in (2.8).

$$\begin{aligned}
\Delta z_{W,L} &= A_{3,3}\Delta F_{Z,L} + A_{3,9}\Delta F_{Z,R} \\
\Delta z_{R,L} &= A_{R,Z}\Delta F_{Z,L} \\
\Delta L_{H,L} &= \frac{1}{k_H}\Delta F_{Z,L} \\
\Delta z_{W,R} &= A_{9,3}\Delta F_{Z,L} + A_{9,9}\Delta F_{Z,R} \\
\Delta z_{R,R} &= A_{R,Z}\Delta F_{Z,R} \\
\Delta L_{H,R} &= \frac{1}{k_H}\Delta F_{Z,R}
\end{aligned} \tag{2.8}$$

Equation (2.8) is then substituted into (2.7) and the results are written in matricial form, highlighting the dependence between vertical irregularity vector and the force vector.

$$\begin{bmatrix} z_{irr,L} \\ z_{irr,R} \end{bmatrix} = \begin{bmatrix} A_{3,3} + A_{R,Z} + \frac{1}{k_H} & A_{3,9} \\ A_{9,3} & A_{9,9} + A_{R,Z} + \frac{1}{k_H} \end{bmatrix} \begin{bmatrix} \Delta F_{Z,L} \\ \Delta F_{Z,R} \end{bmatrix} \tag{2.9}$$

It is finally possible to use the same methodology to compute the relationship between the vertical contact forces and vertical axleboxes accelerations $\ddot{z}_{A,L}$ and $\ddot{z}_{A,R}$.

$$\begin{bmatrix} \ddot{z}_{A,L} \\ \ddot{z}_{A,R} \end{bmatrix} = -\Omega^2 \begin{bmatrix} z_{A,L} \\ z_{A,R} \end{bmatrix} = -\Omega^2 \begin{bmatrix} A_{6,3} & A_{6,9} \\ A_{12,3} & A_{12,9} \end{bmatrix} \begin{bmatrix} \Delta F_{Z,L} \\ \Delta F_{Z,R} \end{bmatrix} \tag{2.10}$$

By combining (2.9) and the inverse of (2.10) the measurement system transfer function is found to be:

$$\begin{bmatrix} z_{irr,L} \\ z_{irr,R} \end{bmatrix} = - \begin{bmatrix} A_{3,3} + A_{R,Z} + \frac{1}{k_H} & A_{3,9} \\ A_{9,3} & A_{9,9} + A_{R,Z} + \frac{1}{k_H} \end{bmatrix} \frac{1}{\Omega^2} \begin{bmatrix} A_{6,3} & A_{6,9} \\ A_{12,3} & A_{12,9} \end{bmatrix}^{-1} \begin{bmatrix} \ddot{z}_{A,L} \\ \ddot{z}_{A,R} \end{bmatrix} \tag{2.11}$$

The transfer function summarised by Equation (2.11) can account for the combined effects of left and right irregularities on both accelerometers. However, it simplifies contact mechanics by imposing a vertical contact direction between wheel and rail. The following subsection will address the implementation of lateral dynamics.

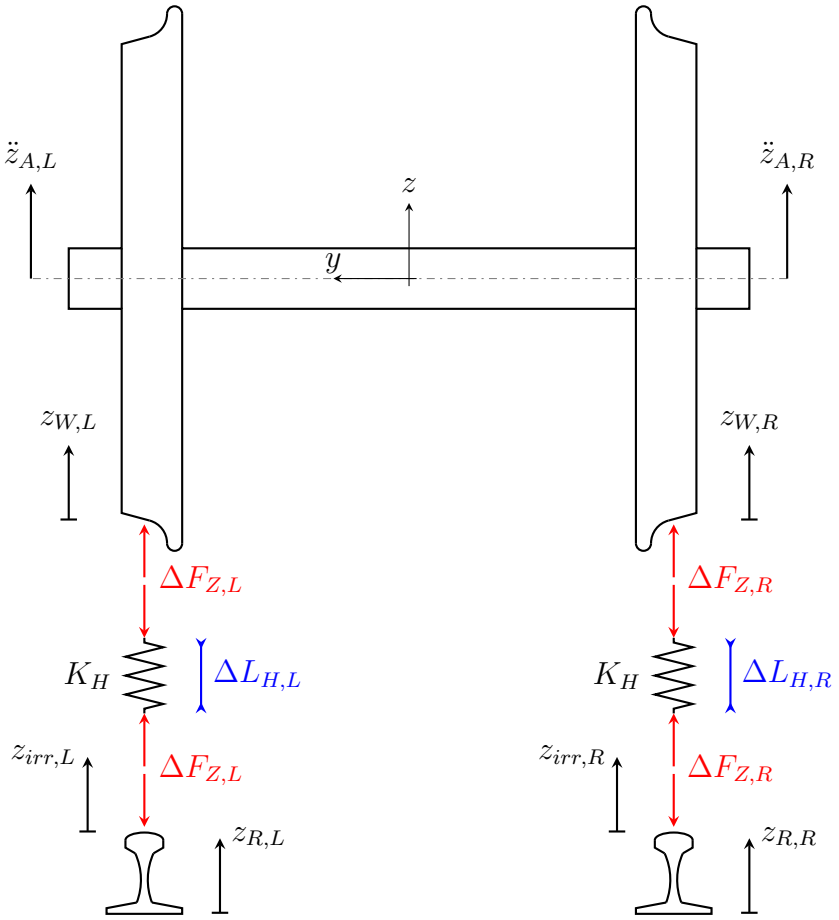

Figure 2.6: Double input design layout.

2.2.3. Vertical and lateral dynamics of the wheelset

In this section, the effect of the inclination of the wheel-rail contact planes are considered. The contact between wheels and rails acts on planes inclined of angle θ_R and θ_L from the horizontal direction respectively. It is therefore necessary to project the force applied in the normal direction with respect to the contact planes into the wheelset's reference system.

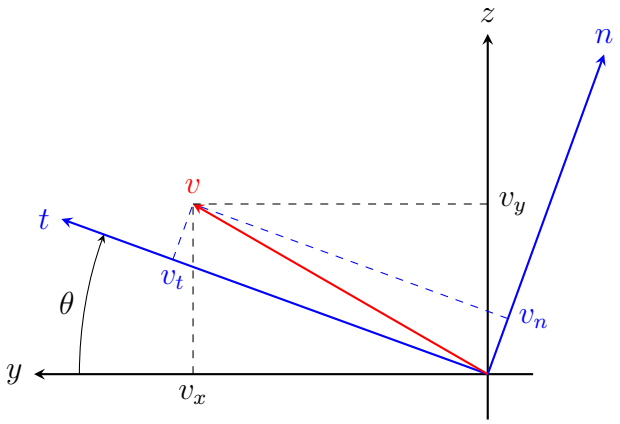

Figure 2.7: Coordinate change reference system.

The passages between the y - z and each t - n reference system are accomplished employing a *change-of-basis matrix* arranged as in equation (2.12). All the sign conventions are highlighted in Figure 2.7.

$$\begin{bmatrix} v_y \\ v_z \end{bmatrix} = \begin{bmatrix} \cos\theta & -\sin\theta \\ \sin\theta & \cos\theta \end{bmatrix} \begin{bmatrix} v_t \\ v_n \end{bmatrix} = [\Lambda(\theta)] \begin{bmatrix} v_t \\ v_n \end{bmatrix} \tag{2.12}$$

If both angles of contact planes θ_L and θ_R are accounted for, any pair of vectors can be converted from the wheelset y - z reference system and the two t - n reference systems of each contact plane and vice versa. This is accomplished by assembling a 4×4 matrix as highlighted in Equation (2.13). This allows to group both left and right irregularity in a single vector as in the previous section, therefore simplifying computations and notation.

$$\begin{bmatrix} v_{y,L} \\ v_{z,L} \\ v_{y,R} \\ v_{z,R} \end{bmatrix} = \begin{bmatrix} \cos\theta_L & -\sin\theta_L & 0 & 0 \\ \sin\theta_L & \sin\theta_L & 0 & 0 \\ 0 & 0 & \cos\theta_R & -\sin\theta_R \\ 0 & 0 & \sin\theta_R & \cos\theta_R \end{bmatrix} \begin{bmatrix} v_{t,L} \\ v_{n,L} \\ v_{t,R} \\ v_{n,R} \end{bmatrix} \tag{2.13}$$

When passing from the y - z wheelset reference system to the two t - n ones, the following passages will be used:

$$\begin{aligned} \underline{v}_{y,z} &= [\Lambda(\theta_L, \theta_R)]\underline{v}_{t,n} \\ \underline{v}_{t,n} &= [\Lambda(\theta_L, \theta_R)]^{\intercal}\underline{v}_{y,z} \end{aligned} \tag{2.14}$$

A schematic representation of the system can be found in Figure 2.8. Forces are not acting anymore in the vertical direction, and each contact plane is characterized by its own angle with respect to direction y. Irregularities in the normal direction on both sides are therefore computed in Equation (2.15), while tangential components, being of

no interest for this work, are discarded.

$$\begin{bmatrix} t_{irr,L} \\ n_{irr,L} \\ t_{irr,R} \\ n_{irr,R} \end{bmatrix} = \begin{bmatrix} \Delta t_{W,L} \\ \Delta n_{W,L} \\ \Delta t_{W,R} \\ \Delta n_{W,R} \end{bmatrix} - \begin{bmatrix} \Delta t_{R,L} \\ \Delta n_{R,L} \\ \Delta t_{R,R} \\ \Delta n_{R,R} \end{bmatrix} + \begin{bmatrix} \Delta t_{H,L} \\ \Delta n_{H,L} \\ \Delta t_{H,R} \\ \Delta n_{H,R} \end{bmatrix} \tag{2.15}$$

It is possible to rewrite the followig relationship in the y - z coordinate system by means of (2.13), therefore obtaining:

$$\begin{bmatrix} t_{irr,L} \\ n_{irr,L} \\ t_{irr,R} \\ n_{irr,R} \end{bmatrix} = \left([\Lambda(\theta_L, \theta_R)]^\intercal \begin{bmatrix} \Delta y_{W,L} \\ \Delta z_{W,L} \\ \Delta y_{W,R} \\ \Delta z_{W,R} \end{bmatrix} - [\Lambda(\theta_L, \theta_R)]^\intercal \begin{bmatrix} \Delta y_{R,L} \\ \Delta z_{R,L} \\ \Delta y_{R,R} \\ \Delta z_{R,R} \end{bmatrix} + \begin{bmatrix} \Delta t_{H,L} \\ \Delta n_{H,L} \\ \Delta t_{H,R} \\ \Delta n_{H,R} \end{bmatrix} \right) \tag{2.16}$$

Wheel and rail receptances can then be used to link each displacement to the contact forces, thus obtaining the matrixes described in Equations (2.17) and (2.18).

$$\begin{bmatrix} \Delta y_{W,L} \\ \Delta z_{W,L} \\ \Delta y_{W,R} \\ \Delta z_{W,R} \end{bmatrix} = \begin{bmatrix} A_{2,2} & A_{2,3} & A_{2,8} & A_{2,9} \\ A_{3,2} & A_{3,3} & A_{3,8} & A_{3,9} \\ A_{8,2} & A_{8,3} & A_{8,8} & A_{8,9} \\ A_{9,2} & A_{9,3} & A_{9,8} & A_{9,9} \end{bmatrix} \begin{bmatrix} \Delta F_{Y,L} \\ \Delta F_{Z,L} \\ \Delta F_{Y,R} \\ \Delta F_{Z,R} \end{bmatrix} = [A_W] \underline{\Delta F}_{Y,Z} \tag{2.17}$$

$$\begin{bmatrix} \Delta y_{R,L} \\ \Delta z_{R,L} \\ \Delta y_{R,R} \\ \Delta z_{R,R} \end{bmatrix} = - \begin{bmatrix} A_{R,Y} & 0 & 0 & 0 \\ 0 & A_{R,Z} & 0 & 0 \\ 0 & 0 & A_{R,Y} & 0 \\ 0 & 0 & 0 & A_{R,Z} \end{bmatrix} \begin{bmatrix} \Delta F_{Y,L} \\ \Delta F_{Z,L} \\ \Delta F_{Y,R} \\ \Delta F_{Z,R} \end{bmatrix} = -[A_R] \underline{\Delta F}_{Y,Z} \tag{2.18}$$

Relative displacement due to the Hertzian contact spring can directly be linked to the contact forces $\underline{\Delta F}_n$ through the following receptance matrix:

$$\begin{bmatrix} \Delta t_{H,L} \\ \Delta n_{H,L} \\ \Delta t_{H,R} \\ \Delta n_{H,R} \end{bmatrix} = \begin{bmatrix} 0 & 0 & 0 & 0 \\ 0 & 1 & 0 & 0 \\ 0 & 0 & 0 & 0 \\ 0 & 0 & 0 & 1 \end{bmatrix} \begin{bmatrix} \Delta F_{t,L} \\ \Delta F_{n,L} \\ \Delta F_{t,R} \\ \Delta F_{n,R} \end{bmatrix} = [A_{H,n}] \underline{\Delta F}_n \tag{2.19}$$

By using these receptances and the force vector in place of wheel and rail displacements

in (2.16), the system is rewritten as:

$$\begin{aligned}\underline{n}_{irr} &= \Big([\Lambda(\theta_L,\theta_R)]^\intercal[A_W]\underline{\Delta F}_{Y,Z} + [\Lambda(\theta_L,\theta_R)]^\intercal[A_R]\underline{\Delta F}_{Y,Z} + [A_{H,n}]\underline{\Delta F}_n\Big) \\ &= \Big([\Lambda(\theta_L,\theta_R)]^\intercal[A_W][\Lambda(\theta_L,\theta_R)] + [\Lambda(\theta_L,\theta_R)]^\intercal[A_R][\Lambda(\theta_L,\theta_R)] + [A_{H,n}]\Big)\underline{\Delta F}_n\end{aligned} \tag{2.20}$$

Equation (2.20) directly links irregularities and forces along the contact direction. The relationship between contact forces and acceleration at the axleboxes is displayed in Equation (2.21). The same procedure used in the previous chapter can be applied, bonding contact forces and axlebox displacements and then deriving the obtained relationship twice using multiplication for $-\Omega^2$ to find axlebox accelerations.

$$\begin{bmatrix}\ddot{y}_{A,L}\\ \ddot{z}_{A,L}\\ \ddot{y}_{A,R}\\ \ddot{z}_{A,R}\end{bmatrix} = -\Omega^2\begin{bmatrix}A_{5,2} & A_{5,3} & A_{5,8} & A_{5,9}\\ A_{6,2} & A_{6,3} & A_{6,8} & A_{6,9}\\ A_{11,2} & A_{11,3} & A_{11,8} & A_{11,9}\\ A_{12,2} & A_{12,3} & A_{12,8} & A_{12,9}\end{bmatrix}\begin{bmatrix}\Delta F_{Y,L}\\ \Delta F_{Z,L}\\ \Delta F_{Y,R}\\ \Delta F_{Z,R}\end{bmatrix} = -\Omega^2[A_B]\underline{\Delta F}_{Y,Z} \tag{2.21}$$

It is finally possible to use Equations (2.20) and (2.21) to obtain the transfer function between rail irregularities and axlebox accelerations:

$$\underline{n}_{irr} = -\left([\Lambda]^\intercal[A_W][\Lambda] + [\Lambda]^\intercal[A_R][\Lambda] + [A_{H,n}]\right)\frac{1}{\Omega^2}\left([A_B][\Lambda]\right)^{-1}\underline{\ddot{X}}_A \tag{2.22}$$

The result of this model is a 4×4 Transfer function matrix, linking both lateral and vertical accelerations of the wheelset to normal irregularities. Tangential irregularities are just a computation byproduct and can be neglected, therefore keeping just the second and fourth term of vector $\underline{n}_{irr}$. The next two chapters expose the detailed computation of the receptances required for this model, while the fifth chapter will describe and compare the results obtained by analyzing acceleration data with these different models.

2.3. Wheelset receptances

When modeling the vehicle's response to rail irregularities, a series of assumptions are postulated. First, the wheelset is assumed to be a *stable system*, i.e. no self-excitation is possible. Moreover, it is assumed that the contributions of the bogies and carbody response can be neglected. The typical range of excitation due to rail irregularities is, in fact, far above the natural frequencies of primary and secondary suspensions, as well as above the frequencies of the rigid motions of the carbody. Therefore it is possible to study only the frequency response of the wheelset and neglect the rest of the vehicle. Data of the

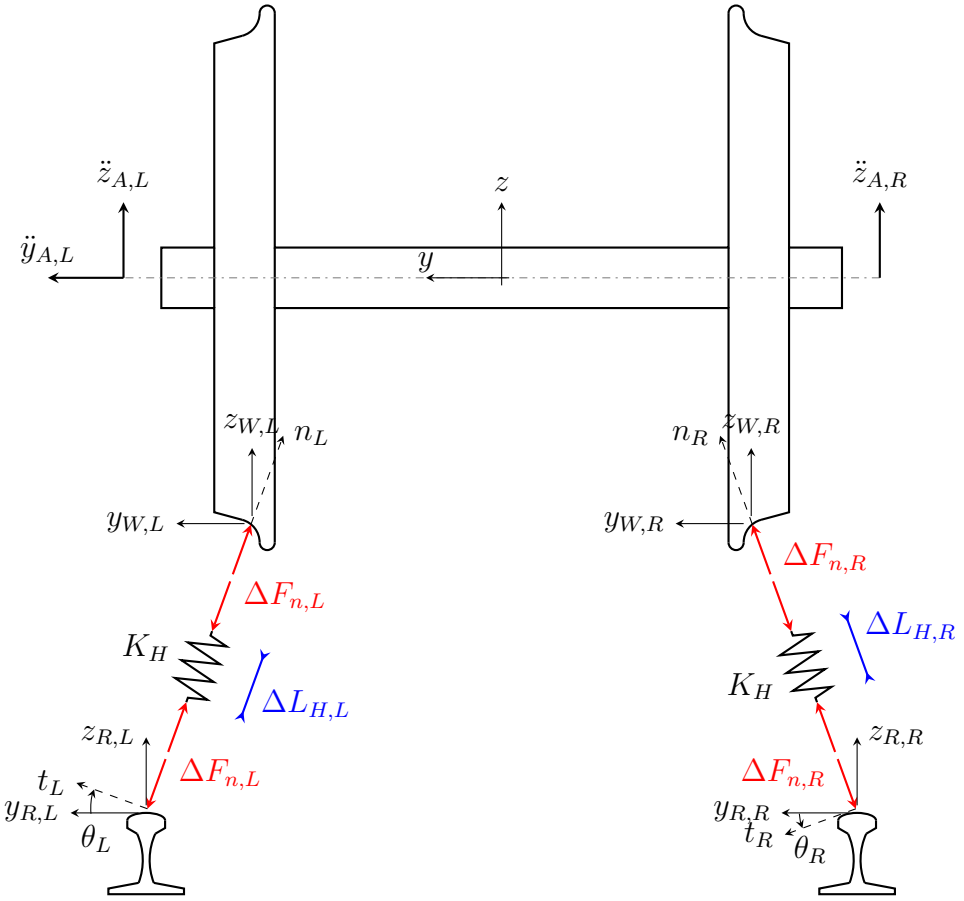

Figure 2.8: Double input design layout with lateral dynamics accounted.

Parameter	Symbol	Value	
Wheelset mass	M_w	1054	kg
Axlebox mass	$M_{axlebox}$	78	kg
Axle mass	M_{axle}	283	kg
Wheel mass	M_{wheel}	251	kg
Brake disk mass	M_{disk}	135	kg
Wheel nominal diameter (new)	R_w	0.41	m
Primary suspension vertical stiffness	$K_{ps,z}$	2×0.5	kN/mm
Primary suspension lateral stiffness	$K_{ps,y}$	2×2.1	kN/mm
Primary suspension longitudinal stiffness	$K_{ps,x}$	2×4.15	kN/mm
Primary suspension vertical damping	$c_{ps,z}$	11	kNs/m
Primary suspension lateral damping	$c_{ps,y}$	50	kNs/m
Primary suspension longitudinal damping	$c_{ps,x}$	85	kNs/m
Wheel profile	[-]	ORE S1002	

Table 2.1: Data of the trailing wheelset of a *Meneghino*.

wheelset under analysis is presented in Table 2.1. Wheelset dynamics are studied using the outputs of a FEM simulation as mode shapes and the results of the experimental campaign described in the following chapters as natural frequencies and damping ratios.

2.3.1. Modal model overview

When computing the dynamic response of a mechanical system, it is often needed to solve complex systems of equations or use a series of Finite Element simulations. Another possibility is the use of a *modal approach*: the key idea behind it is that a flexible body possesses an infinite series of *natural frequencies* or eigenfrequencies, each of them a frequency at which it tends to oscillate when not subjected to external driving forces [24]. Each eigenfrequency will correspond to a *mode shape*, intuitively described as the deformation that a component shows when vibrating at that frequency. Once the mode shapes of a flexible body are known, displacements of its points can be written as a "weighted sum" of all the mode shapes evaluated in the point(s) under analysis. In algebraic terms, mode shapes effectively act as the basis of a reference system described by the matrix $[\Phi]$. Flexible bodies possess infinite mode shapes, but only a finite number n of them will influence their dynamic response in the frequency range under analysis in this work (0-500 Hz). It is therefore possible to neglect all the mode shapes outside this range, transforming the infinite modal base into a finite one. Given a vector of points on the

mechanical system $\underline{x}(t)$ and the modal shapes $\underline{X}^{(1)}$, $\underline{X}^{(2)}$,..., $\underline{X}^{(n)}$, it can be rewritten as:

$$\underline{x}(t) = \begin{bmatrix} x_1 \\ x_2 \\ ... \\ x_n \end{bmatrix}^{(1)} q_1(t) + \begin{bmatrix} x_1 \\ x_2 \\ ... \\ x_n \end{bmatrix}^{(2)} q_2(t) + ... + \begin{bmatrix} x_1 \\ x_2 \\ ... \\ x_n \end{bmatrix}^{(n)} q_n(t) \tag{2.23}$$

where each vector $\underline{x}^{(i)}$ represents the i-th *mode shape* associated with the independent modal coordinate $q_i(t)$. Equation (2.23) can be rewritten more conveniently as:

$$\begin{aligned} \underline{x}(t) &= \underline{X}^{(1)} q_1(t) + \underline{X}^{(2)} q_2(t) + ... \underline{X}^{(n)} q_n(t) \\ &= [\Phi]\underline{q}(t) \end{aligned} \tag{2.24}$$

Conversely, it is possible to pass to the modal coordinates system using the transformation:

$$\underline{q}(t) = [\Phi]^\intercal \underline{x}(t) \tag{2.25}$$

The matrix $[\Phi]$ represents the modal matrix. The dynamic response of an *n-dof* mechanical system can therefore be rewritten in modal coordinates, from:

$$[M]\ddot{\underline{x}} + [C]\dot{\underline{x}} + [K]\underline{x} = 0 \tag{2.26}$$

and, by using the modal coordinates, as:

$$[\Phi]^\intercal [M][\Phi]\ddot{\underline{q}} + [\Phi]^\intercal [R][\Phi]\dot{\underline{q}} + [\Phi]^\intercal [K][\Phi]\underline{q} = 0 \tag{2.27}$$

Modal approach allows writing the equations of motion as a system of n decoupled equations, since the mass, damping and stiffness matrixes becomes diagonal in modal coordinates [24]. However, experimental modal analysis may result in some uncertainties due to errors in accelerometer placement, incorrect impulse inputs, difficulty in exciting some modes, etc. To address this, a 'hybrid' approach can be used: modal frequencies and dampings are identified experimentally while the modal shapes are computed via a Finite Element analysis. The goal of the experimental campaign is to identify the wheelset mode shapes, modal frequencies, and damping ratios, which can then be used to validate and refine the results of the FE analysis. Once the mode shapes of a component are known, the computation of displacements is relatively easy compared to FE analysis. For each point under analysis, receptances can then finally be computed as the superposition of the frequency responses of all the modal shapes.

2.3.2. Receptances calculation

Once the mode shapes matrix $[\Phi]$ is known, it is possible to compute the frequency response function to an external excitation on input i as:

$$(-\Omega^2[\tilde{M}] + i\Omega[\tilde{C}] + [\tilde{K}])\underline{q}_i = [\Phi]^\intercal \begin{bmatrix} 0 \\ \dots \\ F_i \\ 0 \end{bmatrix} \tag{2.28}$$

Where the modal mass, stiffness, and damping matrixes are introduced as:

$$\begin{aligned} [\tilde{M}] &= [\Phi]^\intercal [M][\Phi] \\ [\tilde{C}] &= [\Phi]^\intercal [C][\Phi] \\ [\tilde{K}] &= [\Phi]^\intercal [K][\Phi] \end{aligned} \tag{2.29}$$

From the frequency response in modal coordinates, it is finally possible to find the receptance on direction j as the j-th component of the vector $X_{j,i} = \underline{x}_i^{(j)}$ where $\underline{x}_i$ defined as:

$$\underline{x}_i = [\Phi]\underline{q}_i \tag{2.30}$$

Iterations of Equation (2.28) along all the points of interest defined in Figure 2.5 allow computing the receptances required. Moreover, thanks to the knowledge of modal shapes it is possible to compute the receptance of points which do not belong to the measurement grid.

2.4. Track receptances

In the track section under analysis in this thesis, the rails are directly fastened to the underlying substructure by means of a double elastic layer fastening system. This trackform is called *Milano Modificato* and is widely used in Milano underground network. Rails used in this section are 50E5 rails (whose data come from standard BS EN 13674-1:2011 [25]), whereas the remaining data has been provided by the *Mechanical Engineering Department* of Politecnico di Milano. A summary of all trackform data can be found in Table 2.2. In the following subsections, the track behavior is modeled as an Infinite Timoshenko beam laying on a continuous, double-layer support.

Parameter	Symbol	Value	
Rail mass	m_r	49.9	kg/m
Rail density	ρ_r	7800	kg/m^3
Rail cross-section	A_r	63.62	cm^2
Moment of inertia (y)	$I_{r,yy}$	1844	cm^4
Moment of inertia (z)	$I_{r,zz}$	362.4	cm^4
Young's modulus	E_r	206000	MPa
Poisson ratius	ν_r	0.28	$[-]$
Shear factor	κ_r	0.34	$[-]$
Rail loss factor	η_r	0.02	$[-]$
Support spacing	L_s	0.75	m
Rail-pad vertical stiffness	$K_{rp,z}$	150	kN/mm
Rail-pad vertical damping	$C_{rp,z}$	1.5	kNs/m
Rail-pad lateral stiffness	$K_{rp,y}$	51.71	kN/mm
Rail-pad lateral damping	$C_{rp,z}$	0.75	kNs/m
Rail-pad loss factor	η_{rp}	0.13	$[-]$
Baseplase mass	M_p	15	Kg
Subplate vertical stiffness	$K_{sp,z}$	30	kN/mm
Subplate vertical damping	$C_{sp,z}$	2.8	kNs/m
Subplate lateral stiffness	$K_{sp,y}$	10.3	kN/mm
Subplate lateral damping	$C_{sp,y}$	1.4	kNs/m
Subplate loss factor	η_{sp}	0.20	$[-]$

Table 2.2: Data of the trackform *Milano Modificato*.

2.4.1. Track model

The layout of the track can be appreciated in Figure 2.9. The first layer on which the rail lays represents the rail pad and the second accounts for the elastomeric subplate, while the metallic base plate in between is modeled as a rigid mass. The Timoshenko beam model is chosen since it allows to take into account the effects of shear deformation, which become increasingly important at higher frequencies [26]. There are some assumptions to be made in the analytical model:

- Displacements are infinitesimally small;
- The two rails are considered dynamically decoupled (this is true due to the particular structure of the track, while the presence of concrete or wooden sleepers would cause the two rails to be coupled);
- Longitudinal dynamics are neglected due to the large track impedance;
- The load applied on the rails is considered fixed at $x = 0$, therefore neglecting contributions related to moving loads on the beam;
- Stiffnesses and dampings can be assumed as continuously supporting the rail, therefore neglecting the discrete spacing of rail supports. This forces to neglect the periodic variation of stiffness which is exhibited by discretely-supported tracks;
- The inclination of the rail is neglected and the load is applied on the rail neutral axis, allowing to decouple of vertical and lateral dynamics of the track. This is a strong simplification, since loads misaligned with respect to the neutral axis tend to cause rotations of the rail cross sections, therefore coupling vertical and lateral dynamics.

A procedure to evaluate the receptances of a similar layout has been described by Thompson in [26]. Both layers and the rail possess a damping component given in the form of a loss factor η. This allows for modeling their hysteretic behavior. From these values, it is possible to compute the complex elastic modulus of the rail as:

$$\begin{aligned} E_r^* &= E_r(1 + j\eta_r) \\ G_r^* &= \frac{E_r^*}{2(1 + \nu_r)} \end{aligned} \tag{2.31}$$

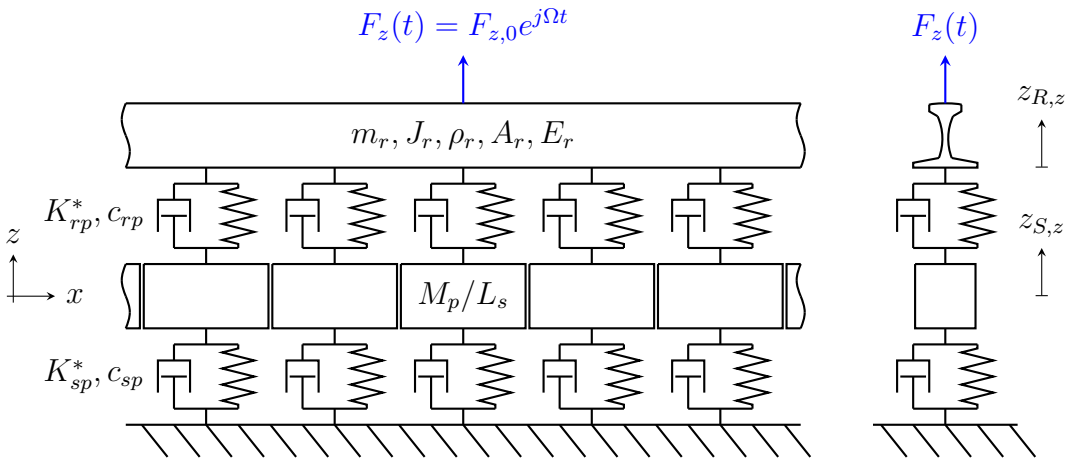

Figure 2.9: Scheme of the track.

The complex stiffnesses per unit length of the two support layer can be similarly modeled using the loss factor as:

$$\begin{aligned} k^*_{rp} &= \frac{K_{rp}}{L_s}(1 + j\eta_{rp}) \\ k^*_{sp} &= \frac{K_{sp}}{L_s}(1 + j\eta_{sp}) \end{aligned} \tag{2.32}$$

Where all data refers alternatively to damping ratios and stiffnesses along the vertical or lateral direction alternatively. Equation (2.33) describes the motion of the system with respect to the vertical displacement of the rail $x_{R,z}$ and the rotation of the rail cross-section around its neutral axis Φ:

$$\begin{cases} m_r\ddot{x}_{R,z} + k^*_{eq}x_{R,z} + G^*_r A_r \kappa_r \dfrac{\partial}{\partial x}\left(\Phi - \dfrac{\partial x_{R,z}}{\partial x}\right) = F_z(t)\delta(x) \\ \rho I_r \ddot{\Phi} - E^*_r \dfrac{\partial^2 \Phi}{\partial x^2} + G^*_r A_r \kappa_r \left(\Phi - \dfrac{\partial x_{R,z}}{\partial x}\right) = 0 \end{cases} \tag{2.33}$$

k^*_{eq} represents the equivalent stiffness per unit of length of the two support layers and can be computed as follows:

$$k^*_{eq} = \frac{\left(k^*_{rp} + j\Omega\dfrac{C_{rp}}{L_s}\right)\left(k^*_{sp} + j\Omega\dfrac{C_{sp}}{L_s} - \Omega^2\dfrac{M_P}{L_s}\right)}{k^*_{rp} + k^*_{sp} + j\Omega\left(\dfrac{C_{rp}}{L_s} + \dfrac{C_{sp}}{L_s}\right) - \Omega^2\dfrac{M_P}{L_s}} \tag{2.34}$$

The solutions to (2.33) can be computed by imposing a harmonic motion as the free solution, as previously done for the wheel receptance:

$$\begin{aligned} x_{R,z}(x,t) &= X_{R,z0}e^{-jkx}e^{j\Omega t} \\ \Phi(x,t) &= X_{R,z0}\Psi e^{-jkx}e^{j\Omega t} \end{aligned} \tag{2.35}$$

The free solutions described in (2.35) are characterized by complex amplitudes $X_{R,z0}$ and $X_{R,z0}\Psi$. k is the complex wavenumber, whose real part represents the phase change per unit distance and the imaginary part represents the distance decay. $\delta(x)$ is the Kroneker's delta. It is possible to solve this system of equations and obtain the rail's vertical and lateral receptances.

2.4.2. Results and validation

Figures 2.10 and 2.11 represent the track vertical and lateral receptances obtained via the infinite, double-supported Timoshenko beam model. It is possible to see the first track resonance frequencies, at around 112 Hz in the vertical direction and 67 Hz in the lateral one. These frequencies correspond to the in-phase resonance of the rail and base plate over the railpad. The second lateral resonance frequency is placed at 374 Hz, where the rail is stationary and the plate moves laterally. Other resonances, corresponding to the higher modes of the track, fall outside the frequency range of the thesis (0-500 Hz). However, the Timoshenko continuously supported infinite beam is not able to take into account the effect of supports spacing. This track characteristic is the source of the Pinned-Pinned resonance, which manifests itself at around 400-1200 Hz [6]. Faccini et al. in [11] offer validation of this approach via a comparison of the Analytical receptance to the receptance obtained by means of an impact test performed on a real track section, in correspondence of a rail support. Results can be appreciated in Figure 2.12.

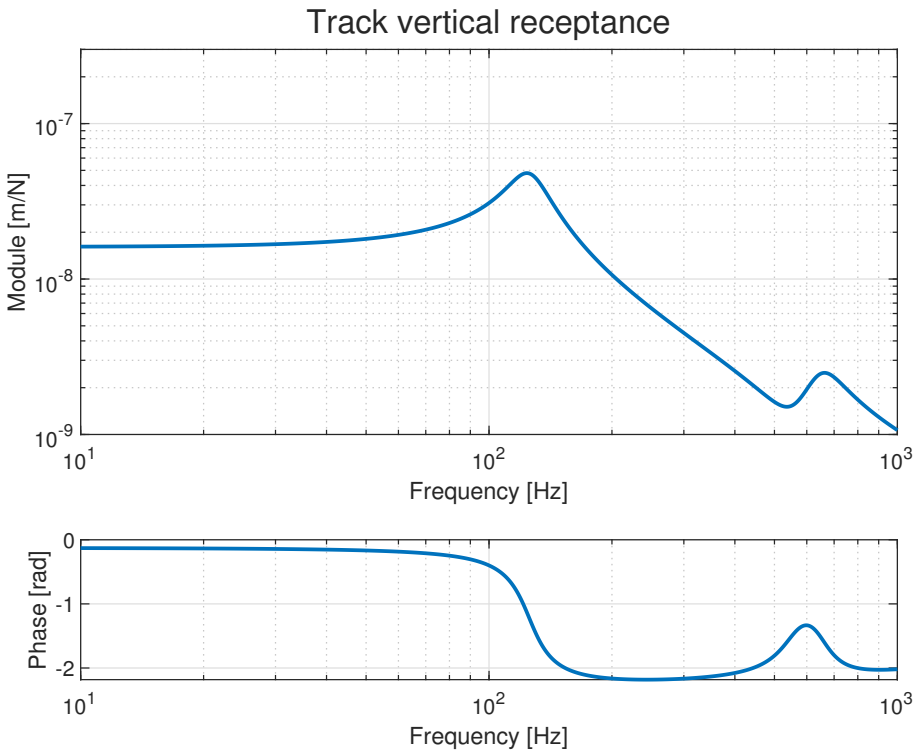

Figure 2.10: Vertical receptance of the track.

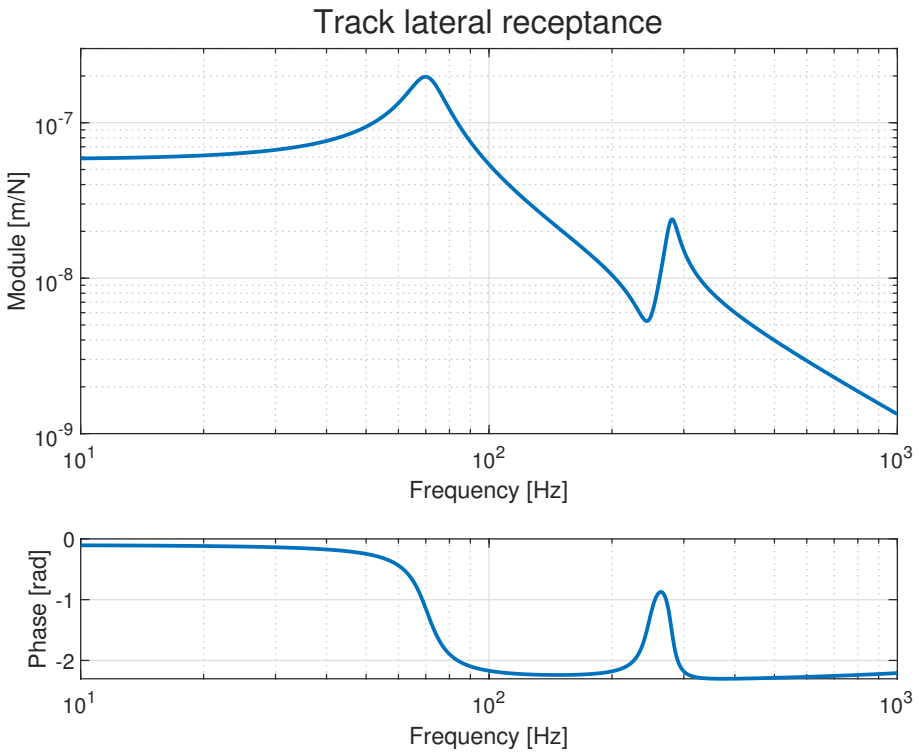

Figure 2.11: Lateral receptance of the track.

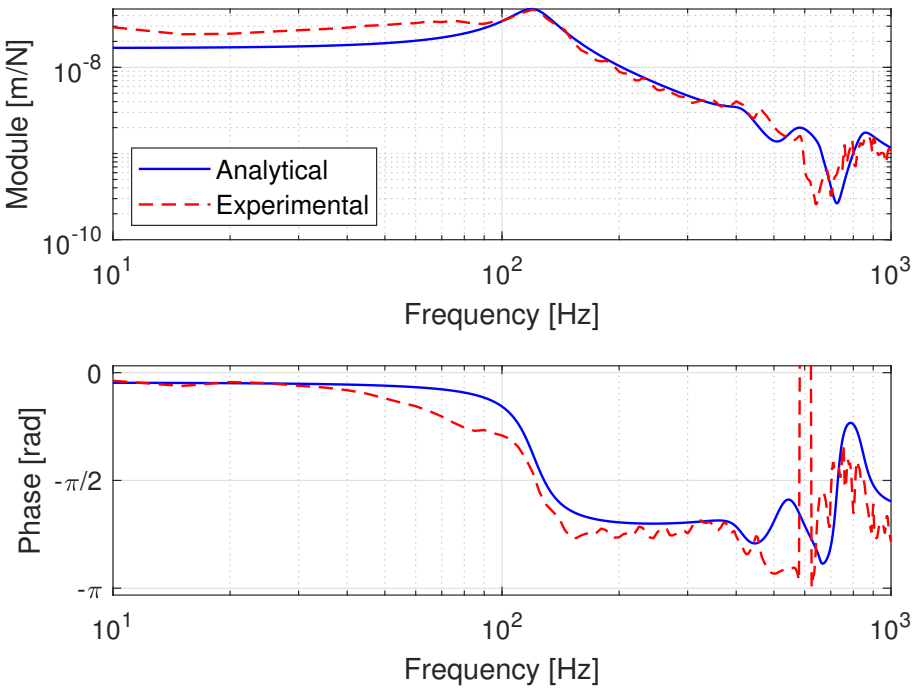

Figure 2.12: Analytical and experimental vertical track point receptance in correspondence of support (from [11]).

3 | Experimental Modal Analysis of the Wheelset

In this chapter, the experimental campaign carried out in order to identify the modal parameters of the wheelset is described. The methodology used in the campaign and the theoretical background behind experimental modal identification are exposed. Modal frequencies, mode shapes, and dampings of the wheelset are identified. Data from the experimental campaign is then compared to the results from a Finite Element Model of the wheelsets. The modal shapes of the wheelset obtained via the FEM analysis are then paired with the corresponding experimental frequencies. The wheelset's receptances are computed and compared to the experimental results.

3.1. Experimental campaing overview

The experimental campaign to identify the modal parameters of the wheelset was carried out in the laboratories of the Mechanical Engineering Department of Politecnico di Milano. A wheelset of the same model used in the instrumented train described in Chapter 2 was instrumented using a series of accelerometers and subjected to a series of impact tests. Although there are different methods that can be employed to estimate the transfer function of a mechanical system [27], it was chosen to use an *impact hammer* over other excitation techniques since impulse excitation is able to excite almost all the relevant frequencies under analysis in the wheelset. The experimental setup can be appreciated in Figure 3.1. During the tests, the wheelset is decoupled from the ground by means of two sets of springs attached to the laboratory's bridge crane. This arrangement is used to simulate the conditions of a free wheelset and ease the need of modelling complex ground constraints. A detailed view of the suspension system and the placement of accelerometers are highlighted in Figure 3.2.

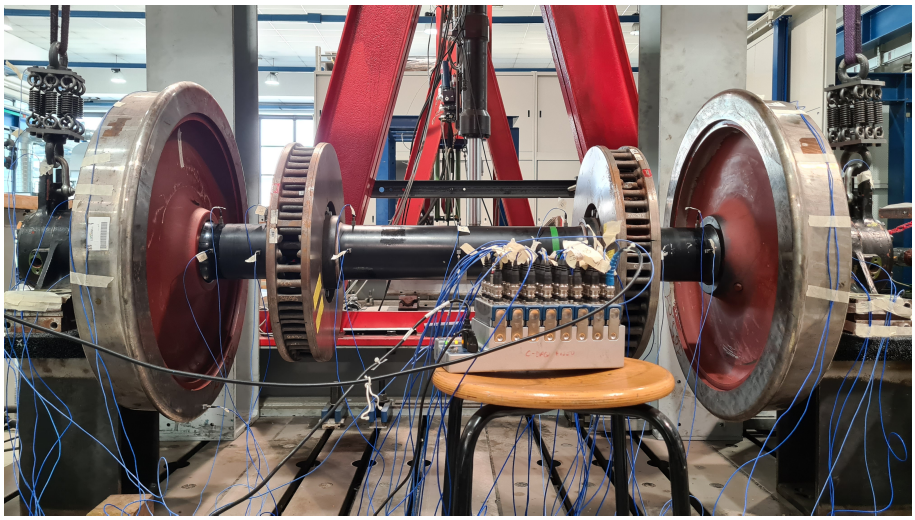

Figure 3.1: Experimental setup used for modal analysis.

(a) Springs suspension system.

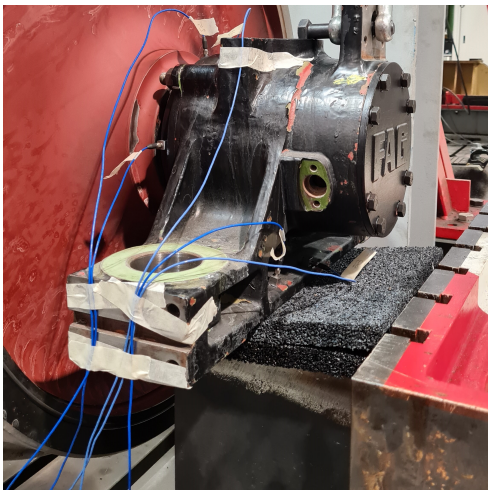

(b) Accelerometers placement detail.

Figure 3.2: Details of suspension system and accelerometers placement.

3.2. Setup

A total of 30 channels are recorded during each test, 29 being used for the accelerometers and one for the impact hammer. Accelerometers are placed on the wheelset as represented in Figure 3.3 to correctly identify both axle and wheels' deformations. Although it would be theoretically possible to compute the receptances needed for the computations exposed in Chapter 2 using only sensors placed at the wheels' contact points and axleboxes, it was decided to instrument the whole wheelset to properly identify all the relevant modes of vibration. Since torsional vibrations can act as a wavelength-fixing mechanism [12],

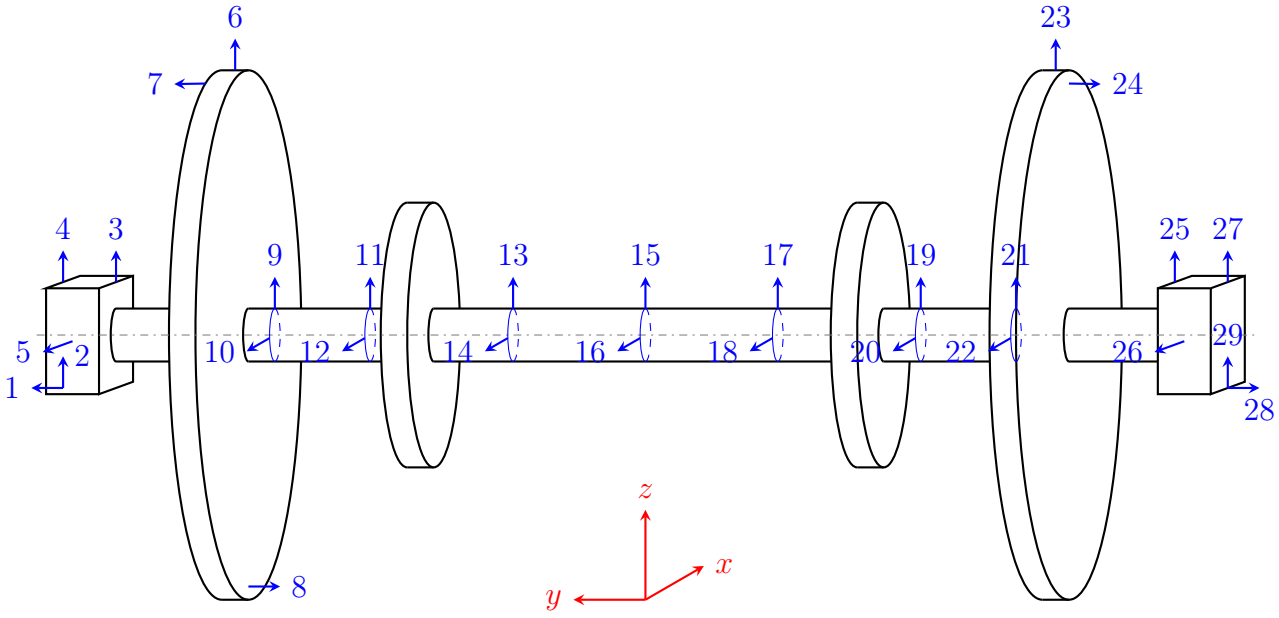

Figure 3.3: Experimental accelerometers setup: flessional modes identification.

identification of torsional modes is also accomplished by means of a second set of impact tests. In order to do so, the accelerometers are repositioned with their measuring direction placed tangentially. Accelerometers on the axleboxes are not repositioned due to the axleboxes bearings decoupling the torsional dynamics of the wheelset from the axleboxes. The resulting layout can be appreciated in Figure 3.4. Impulses are given to the wheelset by using a notch present on the disk brakes. For each test, all the channels are sampled at a frequency of 12800 Hz, stored, and analyzed by using a dedicated Matlab script.

3.3. Frequency Response Functions

The frequency response functions between the input force and output accelerances are estimated using power spectral densities. Given the fact that, in the frequency domain,

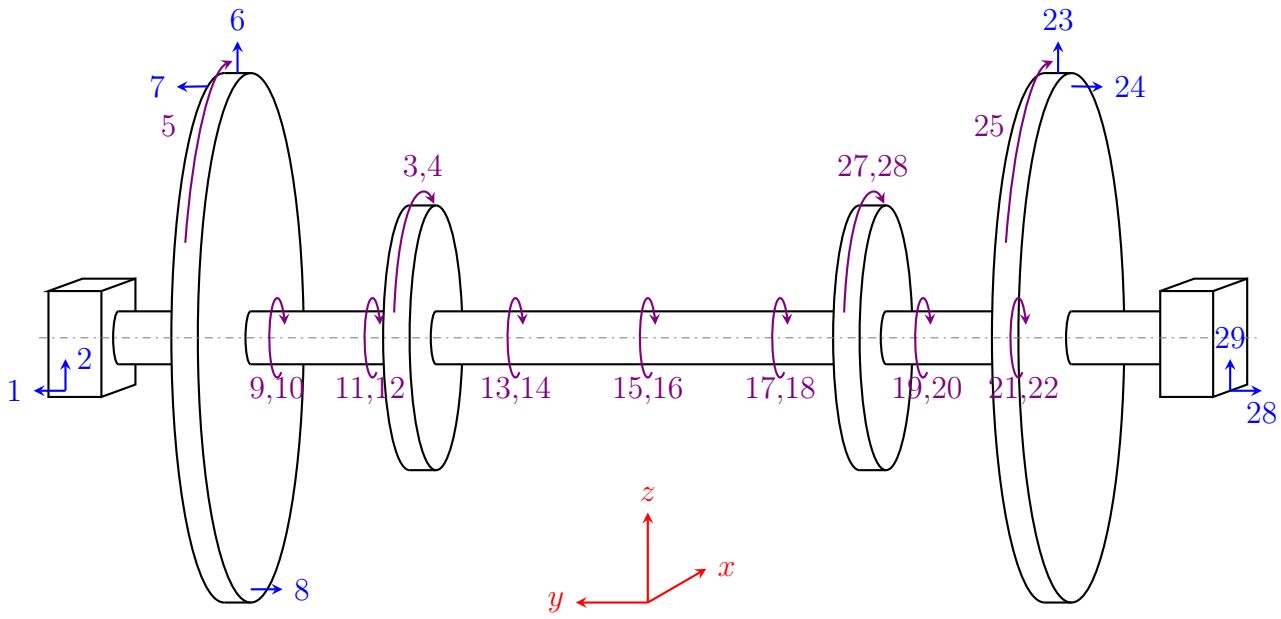

Figure 3.4: Experimental accelerometers setup: torsional modes identification.

the relationship between the input x and the output y is modeled by the linear, time-invariant transfer function $H(f)$ such as:

$$Y(f) = H(f)X(f) \tag{3.1}$$

Assuming that measurement noise is not correlated with the system input, it is possible to estimate the transfer function as:

$$H_1(f) = \frac{P_{y,x}(f)}{P_{x,x}(f)} \tag{3.2}$$

where $P_{y,x}(f)$ is the cross power spectral density between input x and measured output y while $P_{x,x}(f)$ is the power spectral density of the input x. This procedure is iterated throughout all the measured channels to compute the outputs' Frequency Response Functions.

3.4. Modal parameters identification

After obtaining the transfer function, it is possible to identify natural frequencies, damping ratios, and mode shapes using techniques exposed in [24] and [27]. When analyzing the transfer function $h_{j,k}(\Omega)$ between input k and output j, natural frequencies can be identified as those frequencies $\Omega = \omega_i$ at which the transfer functions exhibit a peak in

f (Exp.)	f (FEM)	Damping ratio	Notes	Figure
71 Hz	72 Hz	0.141%	First torsional mode	3.5
72 Hz	71 Hz	0.428%	First flessional mode	3.6
128 Hz	119 Hz	0.098%	Second flessional mode	3.7
195 Hz	176 Hz	0.129%	Third flessional mode	3.8
221 Hz	195 Hz	0.052%	First wheel mode	3.9
270 Hz	305 Hz	0.034%	Second Torsional mode	3.10
286 Hz	305 Hz	0.424%	Fourth flessional mode	3.11
322 Hz	380 Hz	0.043%	Fourth torsional mode	3.12
425 Hz	419 Hz	0.011%	Second wheel mode	3.13

Table 3.1: Identified mode shapes.

magnitude. At each resonant frequency, the contribution of the corresponding vibration mode is maximum while the other modes' contributions are less significant, a reasonable assumption in structures characterized by low damping ratios. In this thesis, a *least-squares complex exponential method* was used to estimate modal parameters.

3.5. Results

The experimental analysis is able to successfully identify 9 modal shapes. The identified shapes are then compared to the results coming from a Finite Element modal analysis; the results can be found in Table 3.1. Some of the modal frequencies are identified only during the experimental campaign and have no evidence on the Finite Element model of the wheelset; others are instead only identified in the FEM analysis and had no feedback in the experimental analysis. It is decided to take into account only the modal shapes correctly visualized by both the experimental campaign and FEM approach.

3.5.1. Mode shapes

The system's mode shapes can be appreciated in the Figures below. Each Figure compares the modal shape obtained via a Matlab routine that plots the results of modal identification to the corresponding mode obtained via Finite Element Analysis. All modes have been normalized and scaled to highlight displacement.

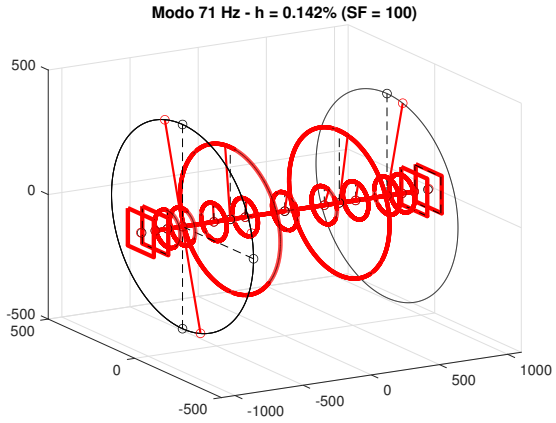

(a) Experimental identification.

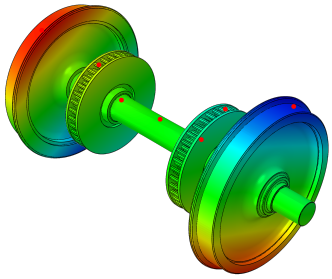

(b) FEM results.

Figure 3.5: First torsional mode.

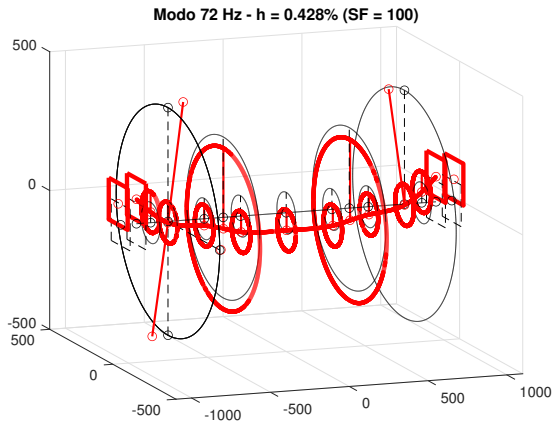

(a) Experimental identification.

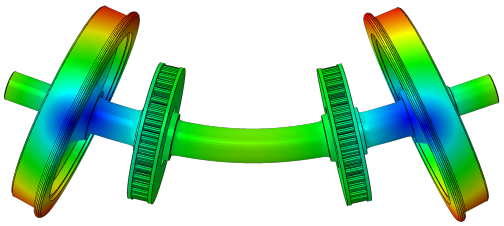

(b) FEM results.

Figure 3.6: First flessional mode.

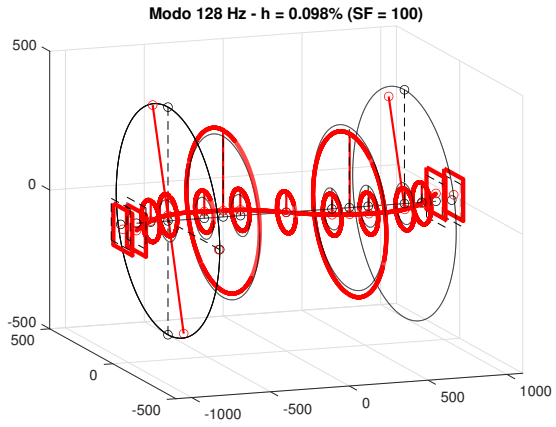

(a) Experimental identification.

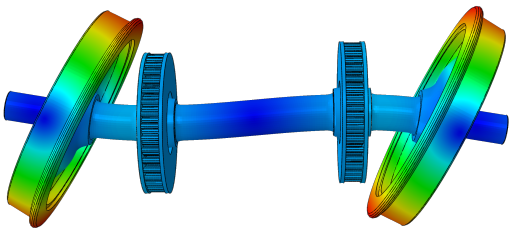

(b) FEM results.

Figure 3.7: Second flessional mode.

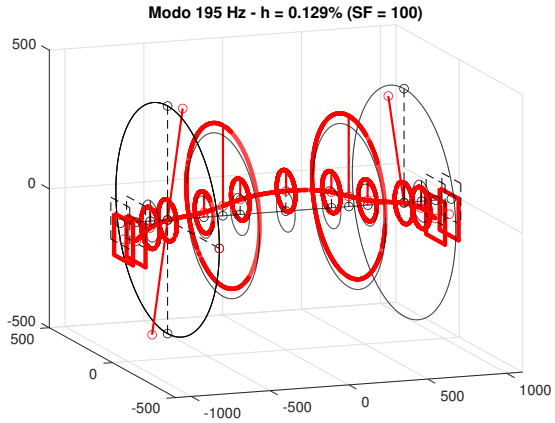

(a) Experimental identification.

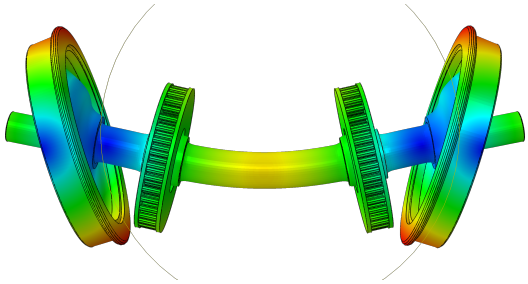

(b) FEM results.

Figure 3.8: Third flessional mode.

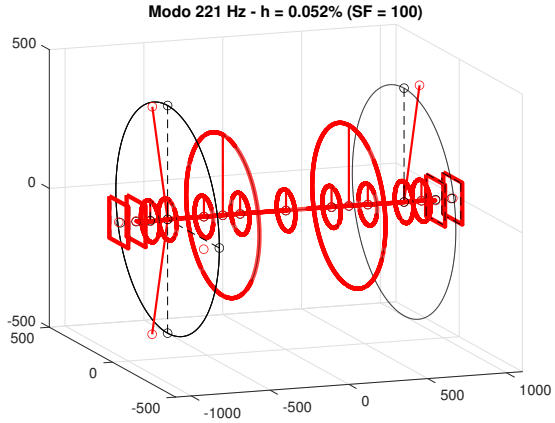

(a) Experimental identification.

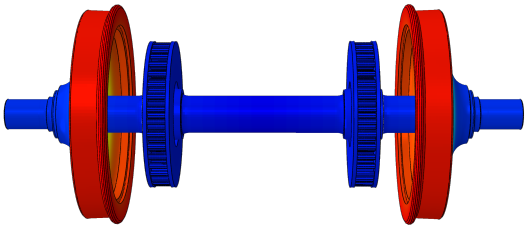

(b) FEM results.

Figure 3.9: First wheel mode.

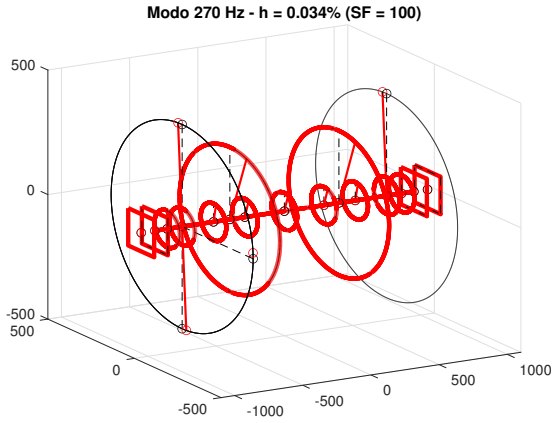

(a) Experimental identification.

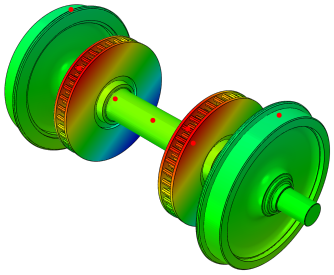

(b) FEM results.

Figure 3.10: Second torsional mode.

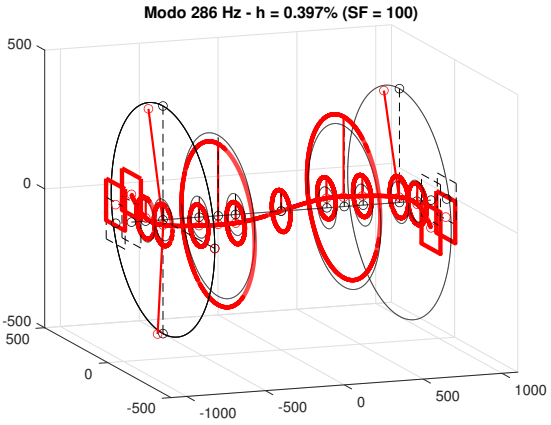

(a) Experimental identification.

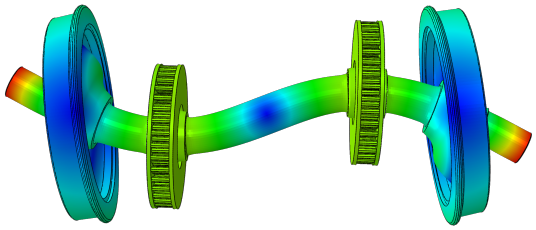

(b) FEM results.

Figure 3.11: Fourth flessional mode.

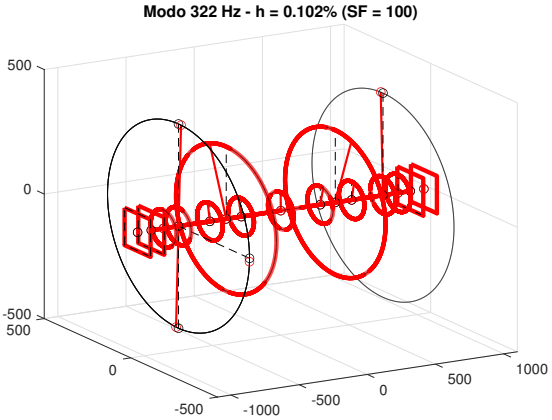

(a) Experimental identification.

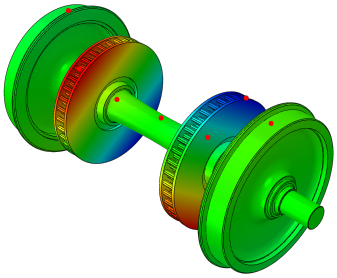

(b) FEM results.

Figure 3.12: Third torsional mode.

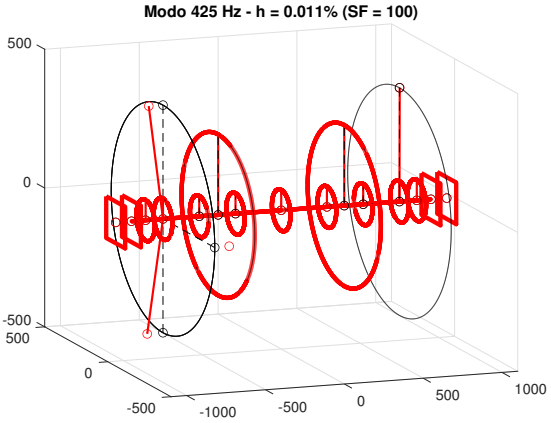

(a) Experimental identification.

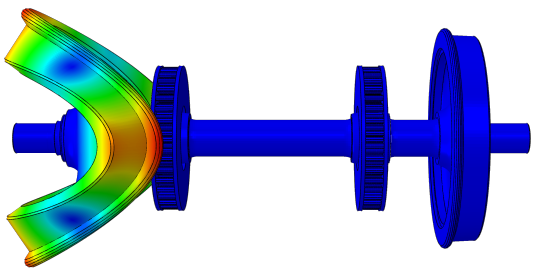

(b) FEM results.

Figure 3.13: Second wheel mode.

3.5.2. Receptances

Finally, the receptances are computed with the procedure followed in Chapter 2. Therefore, the modal frequencies and damping ratios exposed in Table 3.1 are paired with the mode shapes obtained via FEM analysis. This model is then used to compute the receptances highlighted in the following figures. Due to the modal model being symmetric, only half of the receptances are shown, grouped in four figures. For all the figures, the convention adopted is the same as found in Figure 2.5.

- Figure 3.14 shows receptances in vertical direction (input in the left wheel contact point and displacement outputs in vertical direction as well;
- In Figure 3.15 the input is a lateral force in the left wheel contact point and all the outputs are aligned in the lateral direction;
- Figure 3.16 highlights the effects of a lateral force on the wheel contact point on vertical displacements;
- Conversely, Figure 3.17 shows the effects of a vertical force on the wheel contact point on lateral displacements.

The wheelset's rigid displacements and rotations on the primary suspensions are not identified experimentally but are directly accounted for in the Finite Element Model.

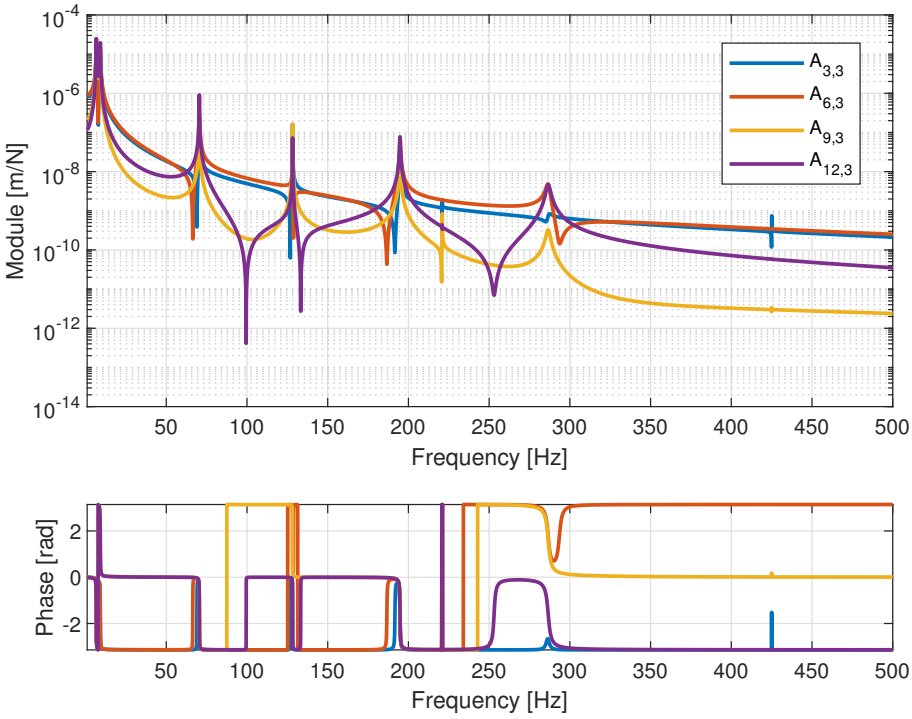

Figure 3.14: Receptances in vertical direction.

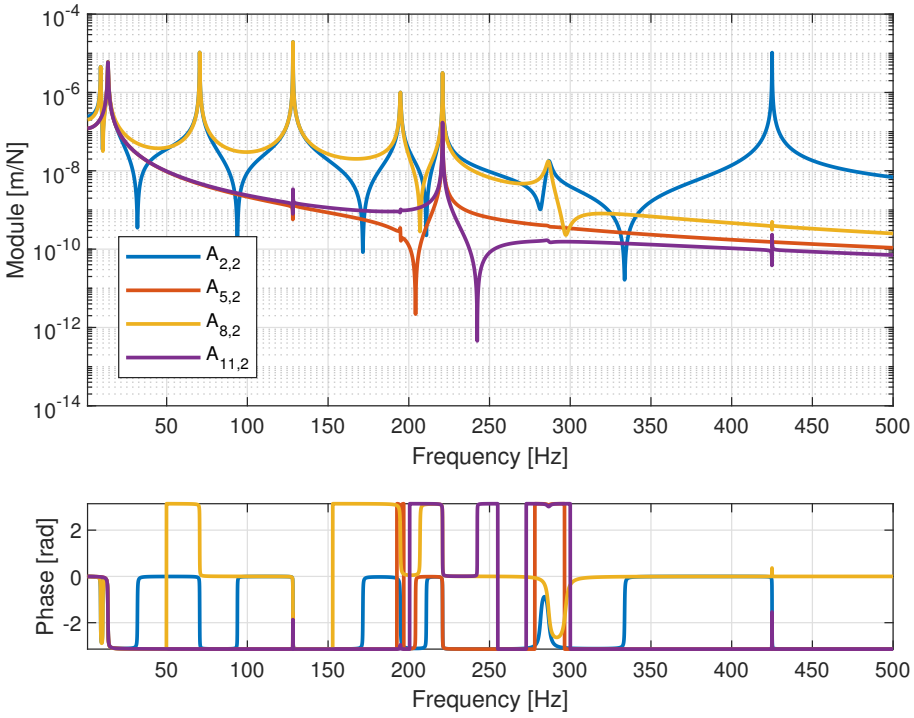

Figure 3.15: Receptances in lateral direction.

3.5.3. Modal model validation

Finally, the results of the modal model are compared with the experimental Frequency Response Functions of the wheelset acquired in the experimental campaign, in order to validate the model's results. Figures 3.18 and 3.19 show that the modal model is able to correctly simulate the actual behavior of the real wheelset in the frequency range of interest.

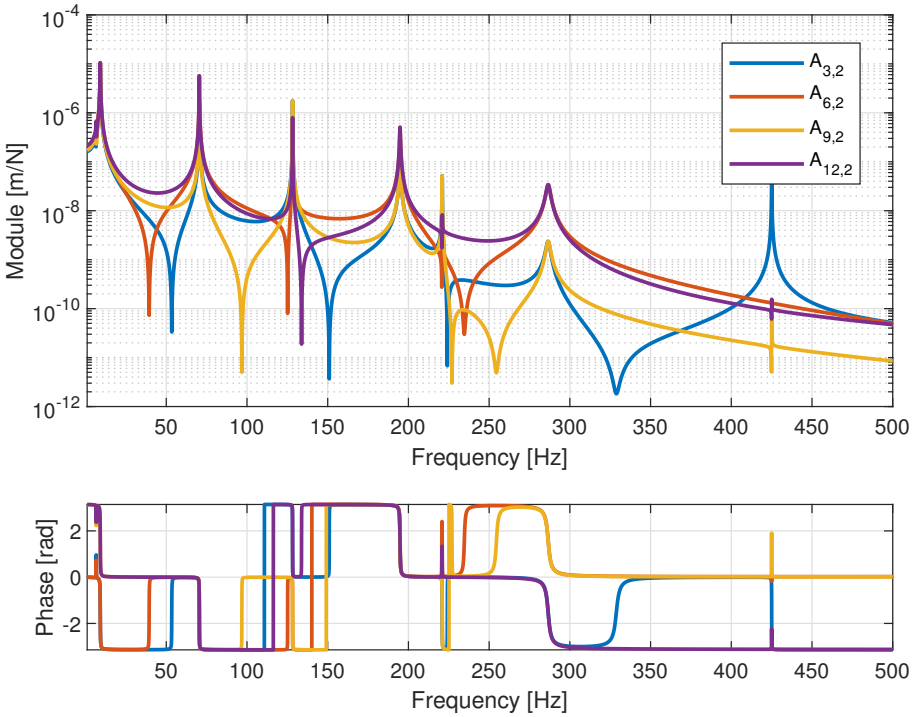

Figure 3.16: Cross receptances: lateral to vertical direction.

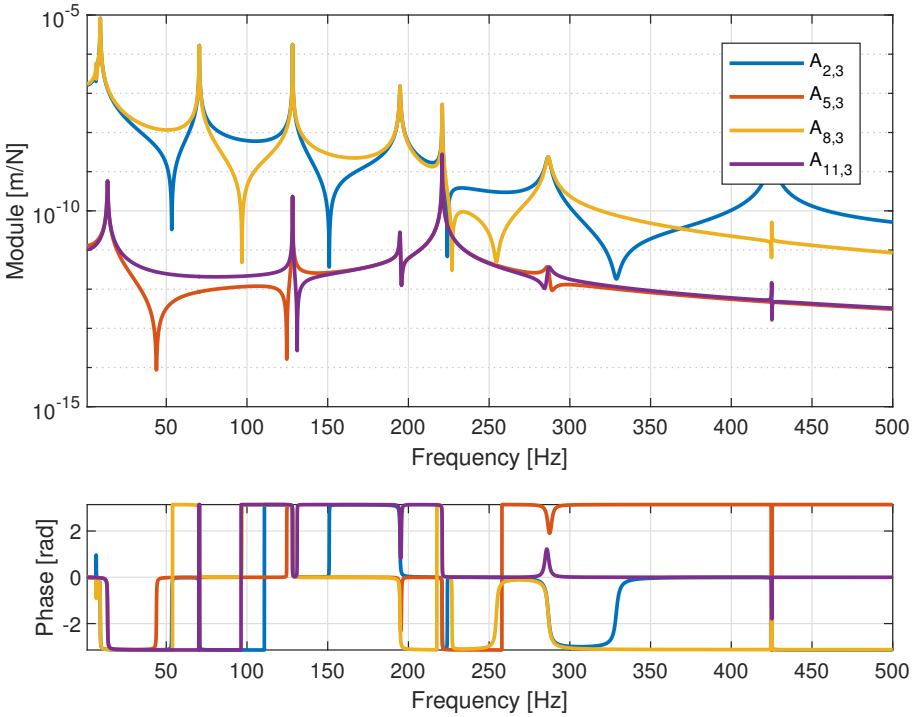

Figure 3.17: Cross receptances: vertical to lateral direction.

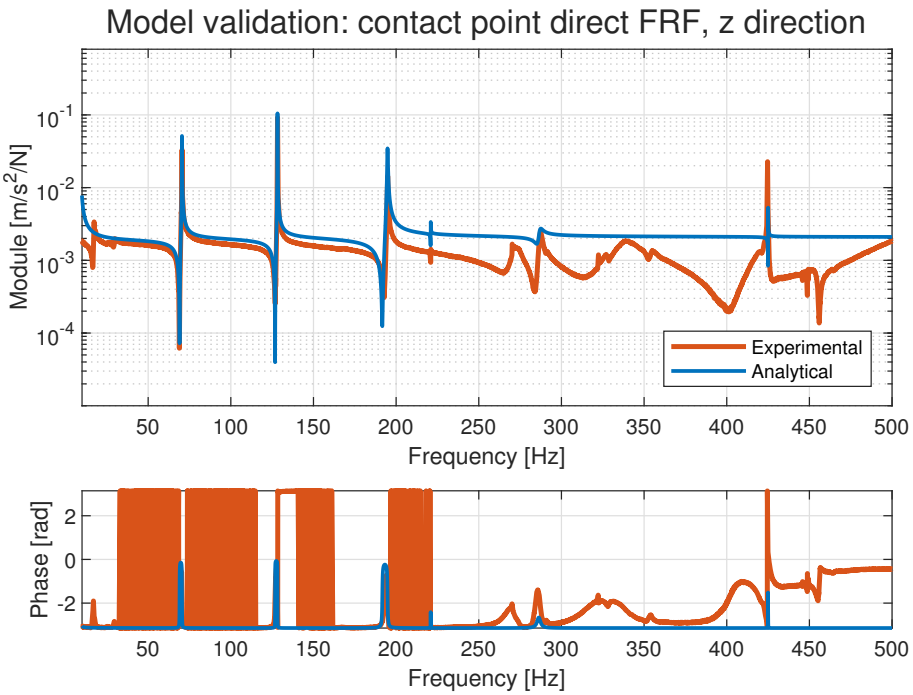

Figure 3.18: Contact point direct FRF validation, vertical direction.

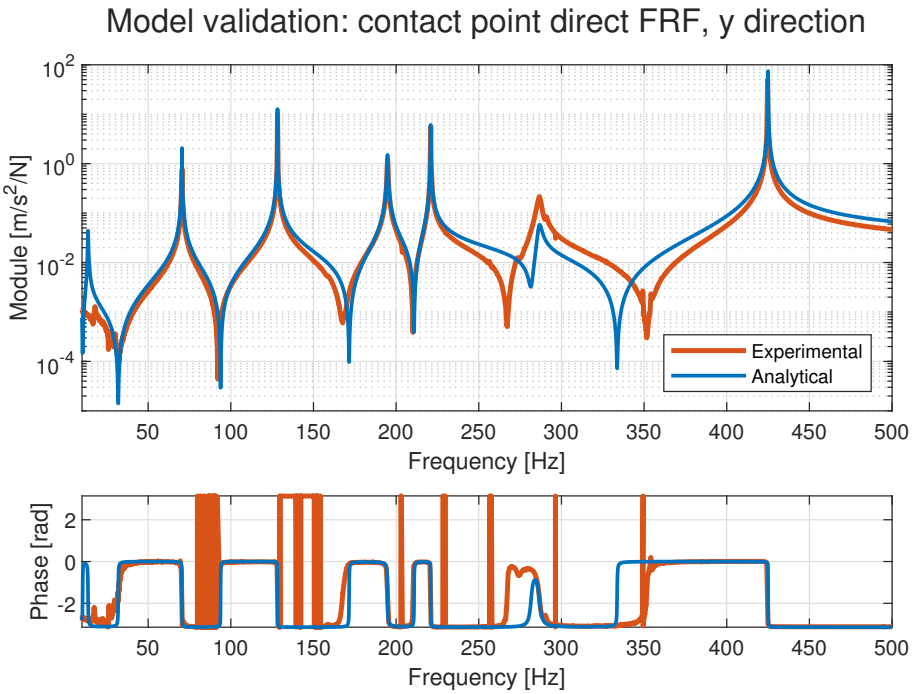

Figure 3.19: Contact point direct FRF validation, lateral direction.

4 | Results

The different wheel-rail interaction models exposed in the previous Chapter are computed and the resulting transfer functions are shown. The robustness of the measurement system is investigated by using artificial roughness profiles, in order to check how changes in modal parameters affect the system's response. The algorithm is then tested by using acceleration measurements collected by the instrumented trainset in Milan's underground network, as presented in Chapter 2. The results of the different wheel-rail interaction models are compared and their robustness is checked. A way to improve the confidence of roughness measurements using the average of multiple tests is validated. The effects of changes in modal parameters of the position of the accelerometers on the axlebox are investigated. Finally, the possibility of following the growth of corrugation over time is discussed.

4.1. Transfer functions of the measurement system

Once the receptances of the wheelset and track are computed as exposed in the previous Chapters, the model of the wheel-rail interaction can be used to compute the transfer function between rail irregularities and axlebox accelerations.

When considering the dynamics of only half of the wheelset, the measurement system neglects any cross contribution between left and right side irregularity, therefore becoming a single-input, single-output system. The receptance between the rail irregularity and the contact force can be computed as exposed in Equation (2.5). The half-wheelset model uses only direct receptances in the vertical direction for both wheel and rail. A representation of all the receptances involved is presented in Figure 4.1. It is possible to appreciate as, at lower frequencies, the dynamics of the system is mainly governed by the wheelset, while the track starts playing a more important role at higher frequencies and the contact stiffness has a uniform contribution at all frequencies. Moreover, the wheel's direct vertical receptance possesses sharp peaks corresponding to resonances, which are translated to the global receptance.

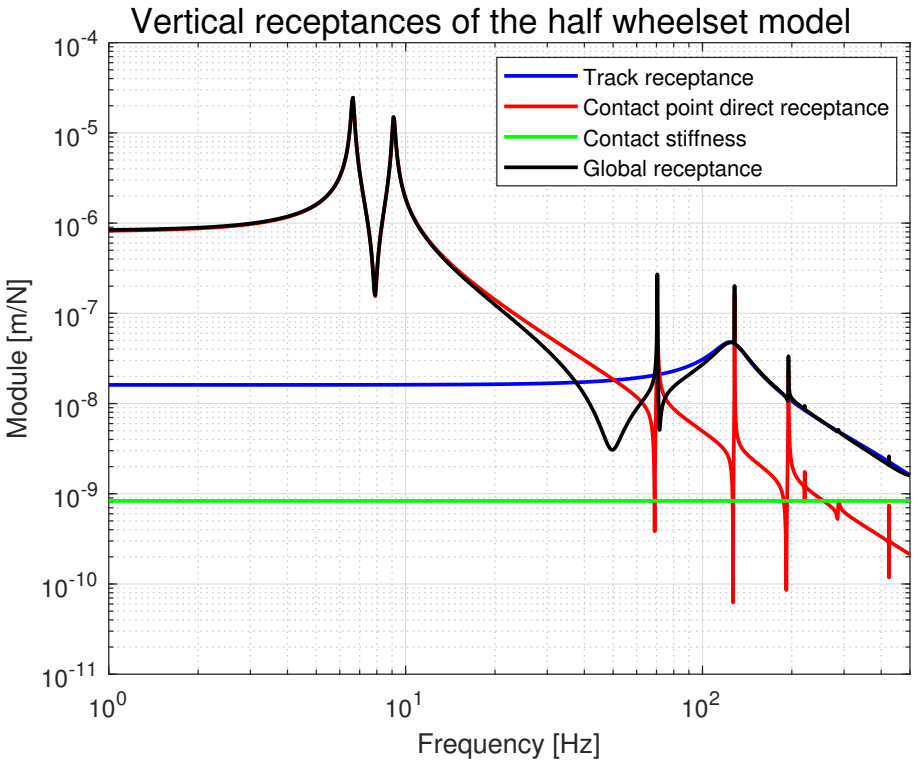

Figure 4.1: Direct vertical receptaces of the half wheelset model.

The first two peaks at 7 and 9 Hz are related to the rigid body motion of the wheelset on the primary suspension, vertical bounce and roll motion respectively. However, these frequencies fall outside the range of interest of corrugation in this thesis, which is in the interval 10-500 Hz. They will therefore have no influence on the overall performance of the measurement system. Adding the contact point-Axlebox vertical receptance it is finally possible to compute the Transfer Function of the measurement system according to Equation (2.6), which is depicted in Figure 4.2. The transfer function presents several peaks, which correspond to the modal frequencies of the system highlighted in Table 3.1.

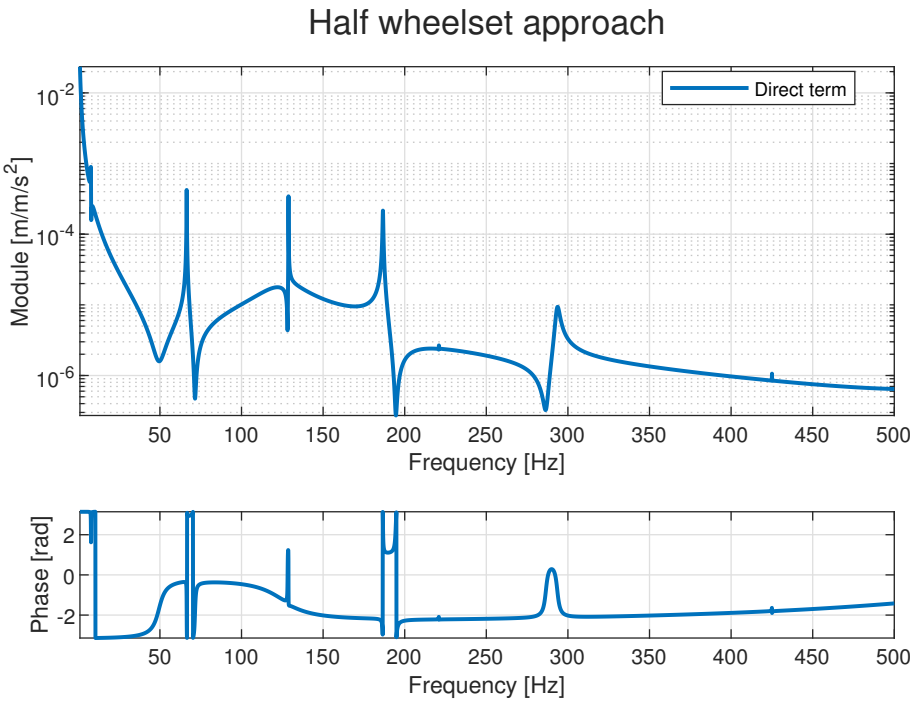

Figure 4.2: Transfer Function of the system: half wheelset.

Equation (2.11) allows the introduction of coupling between the two contact points and axleboxes. The two irregularities are now linked to the two measured accelerations by means of a symmetric, 2×2 matrix. The two direct and the two cross terms are exposed in Figure 4.3: the direct term the same of the results of the half wheelset model. However, as a result of the presence of the cross terms, the acceleration measurements on each accelerometer have a component caused by irregularities on both rails. This can be particularly critical in correspondence to the amplitude peaks of the transfer functions since at these frequencies both direct and cross-term have the same amplitude. The presence of a single accelerometer reading in correspondence of these frequencies would result in the two irregularity profiles being reconstructed with the same amplitude, a large error since corrugation in curves usually appears only on one of the two rails.

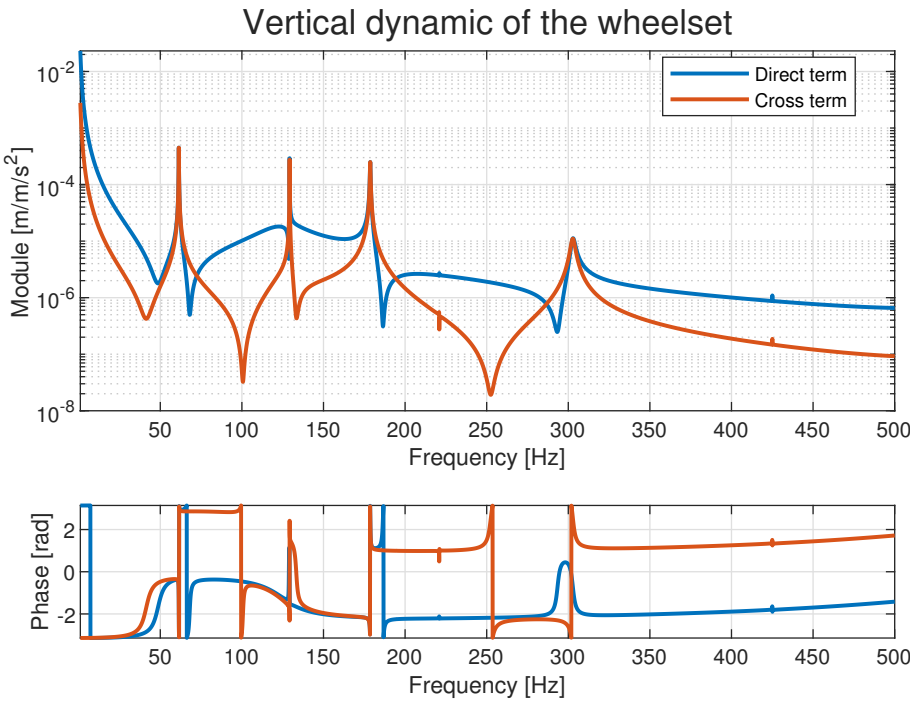

Figure 4.3: Transfer Function of the system: full wheelset, vertical dynamic.

It is finally possible to introduce the effects of the inclination of the contact planes as done in Equation (2.22). The two angles are computed by means of a multibody simulation of the wheelset negotiating the curve under analysis. The presence of inclined contact planes causes a difference in the terms of the Transfer functions matrix, which is not symmetric anymore. This could partially alleviate the problems highlighted with the previous model, allowing to recognize correctly the side at which corrugation appears. The four terms are represented in Figure 4.4. As a matter of fact, it is possible to see the effects of the mode shape at 425 Hz in the terms linking irregularity on the left side to accelerations on the left and right sides. This is due to the lateral component of the contact force exciting that mode.

4.2. Influence of uncertainties on wheelset modal parameters

After computing the system's transfer functions, their robustness to uncertainties is checked. In fact, there are different uncertainties that can influence the reconstruction of irregularity profiles, such as:

- Temperature and ambient condition changes;

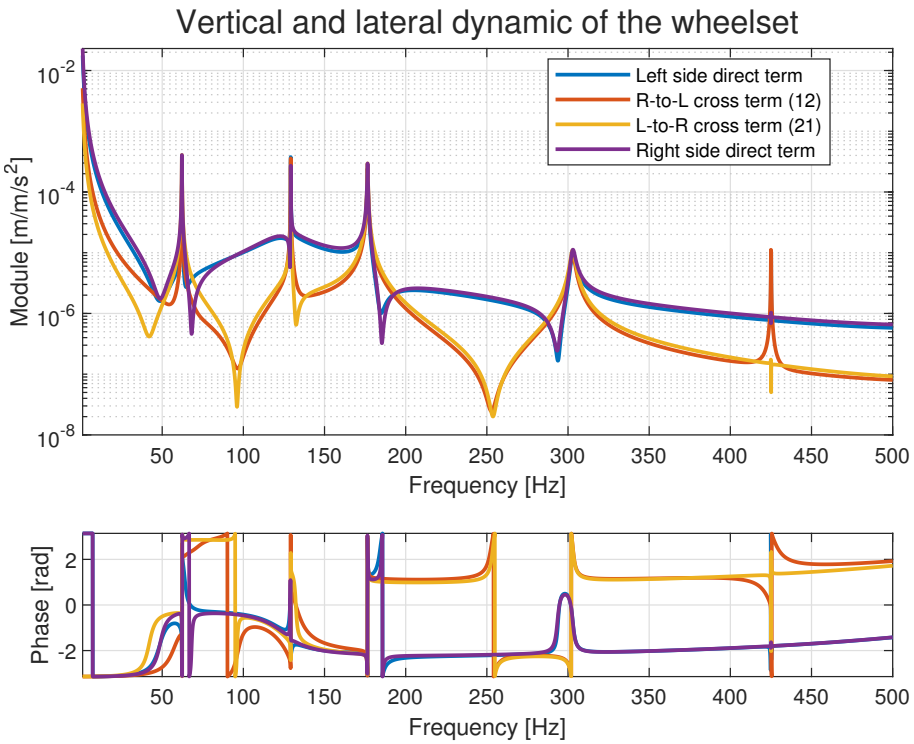

Figure 4.4: Transfer Function of the system: full wheelset, vertical and lateral dynamics.

- The effects of wear and wheel reprofiling;
- Differences between the instrumented wheelsets;
- Errors in the effects of errors in the identification of modal parameters, etc.

Ideally, small changes in modal frequencies and damping ratios should not affect the results, i.e. data coming from two different wheelsets travelling at slightly different speeds should be able to reconstruct similar irregularity profiles. To investigate this, a series of 50 modified transfer functions are constructed, each obtained by randomly varying the modal frequencies and damping ratios of the nominal one by $\pm$ 10%. These variations allow to simulate the effects of uncertainties in the measurement conditions. A test irregularity profile is then assembled, starting from a white noise signal on the left side and a constant profile with no irregularity on the right side: the left side is therefore characterized by a uniform frequency spectrum. These irregularities are converted to the frequency domain by means of a FFT algorithm and their spectra are multiplied by the inverse of the three measurement systems transfer functions, creating three sets of acceleration spectra. These accelerations are then multiplied by the modified transfer functions to obtain a series of irregularity spectra. For each frequency, the standard deviation of the module of the irregularities is computed, with the results highlighted in Figures 4.5, 4.6 and 4.7.

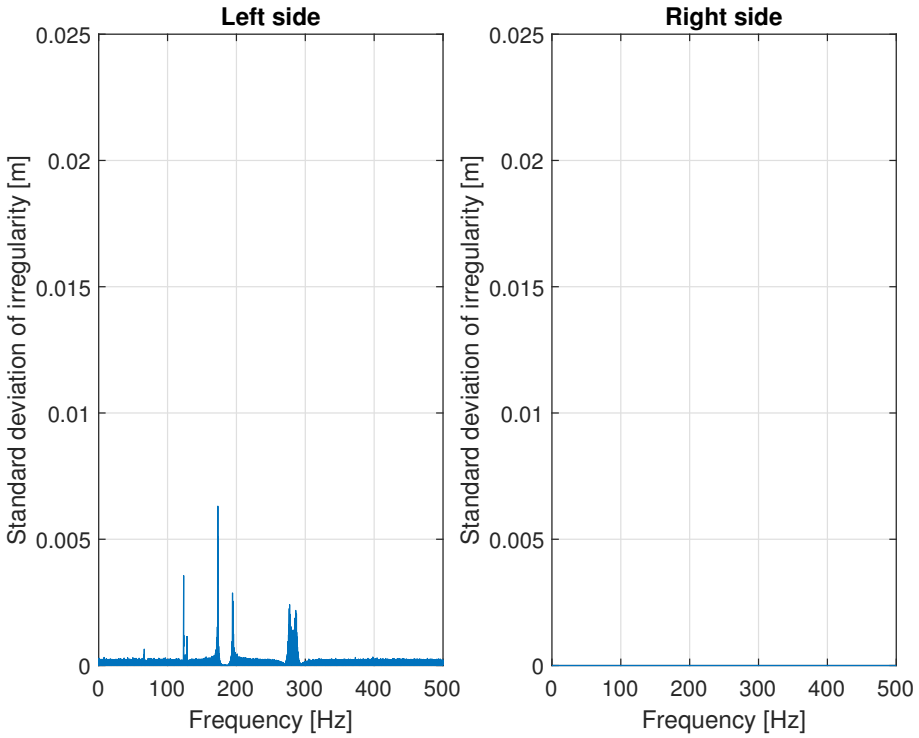

Figure 4.5: Spectral standard deviation: half wheelset.

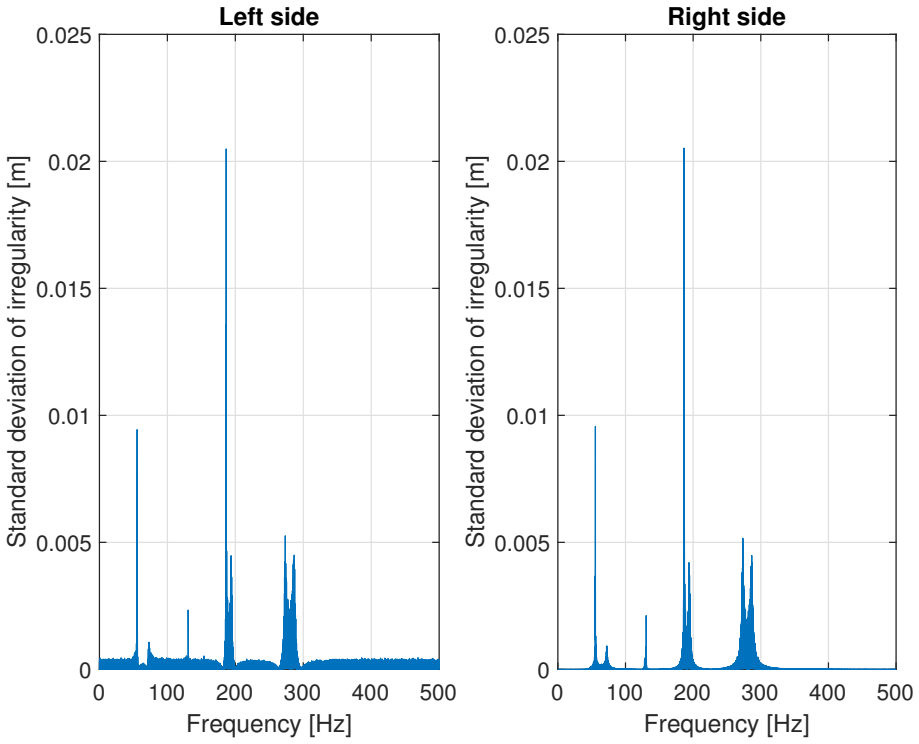

Figure 4.6: Spectral standard deviation: full wheelset, vertical dynamic.

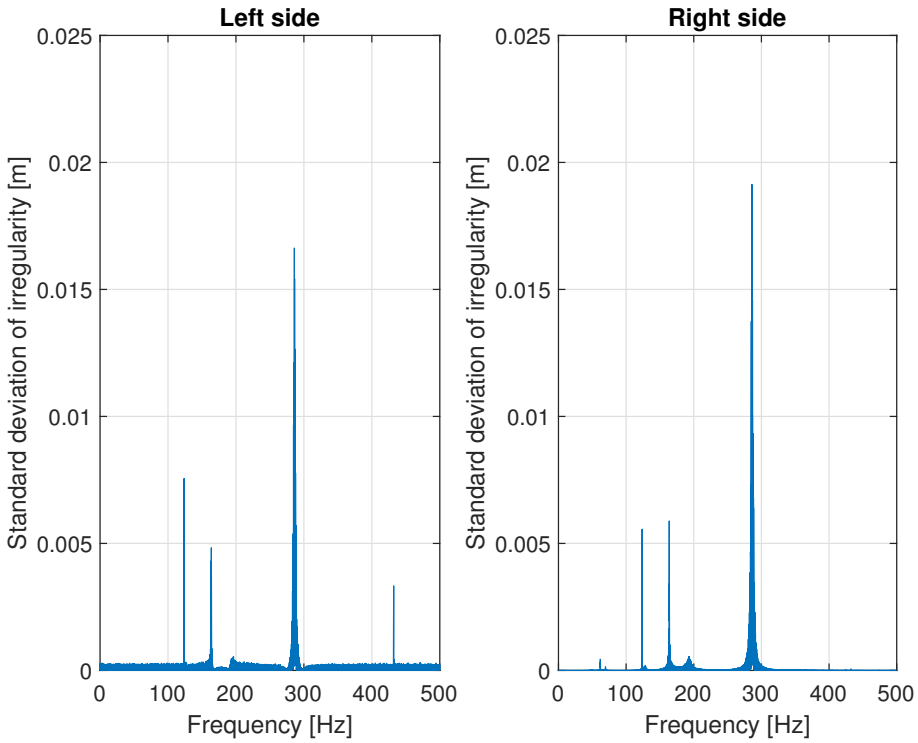

Figure 4.7: Spectral standard deviation: full wheelset, vertical and lateral dynamics.

It is possible to see that the obtained spectral standard deviations are almost constant in large parts of the frequency range. In these regions, the irregularity profiles can be robustly reconstructed even if there are some imprecisions in the modal parameters or if slightly different frequencies are excited (for example, if different measurements are taken at slightly different speeds). Ideally, if no variations in the modal parameters are introduced, the spectral standard deviation is zero at all frequencies. However, there are some frequency ranges in which the spectral variances suddenly increase. These ranges correspond to resonances or antiresonances in the wheelset or rail receptances. Within these ranges, small changes in modal parameters lead to large dispersion in the measurement system's outcomes, severely under- or overestimating irregularity. As a matter of fact, two consecutive passages on the same line section at different speeds may create spectra with large differences in the reconstructed irregularity profiles. Moreover, these frequencies are often associated with some of the wavelength-fixing mechanisms exposed in Chapter 1. Therefore, corrugation is usually present on the tracks at frequencies compatible with the large, aforementioned peaks in dispersion, further exacerbating their correct identification.

4.3. Rail corrugation monitoring

During this thesis, axlebox acceleration data coming from a section of the *M1* line of Milan subway are considered. The section under analysis is characterized by a series of two curves and a switch. Both curves have the tendency of developing corrugation and the section is frequently grinded. Since the instrumented trainset runs along the line almost every day, a large dataset it accessible to study the development of corrugation over time. Figure 4.8 represents the curvature of the line and the acceleration profile measured on corrugated rails.

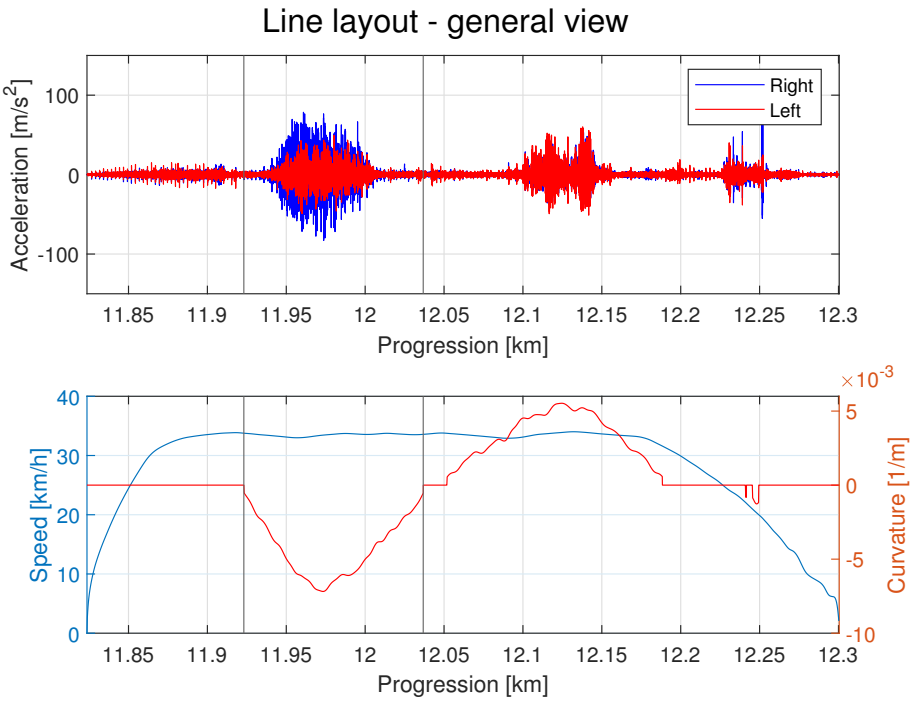

Figure 4.8: *Conciliazione - Pagano*: line layout.

The analysis of the following sections is concentrated in the first curve of the section, in which the contact plane angles between wheel and rails have been computed. The curve is highlighted by the vertical lines in Figure 4.8.

4.3.1. Synthetic indexes for roughness monitoring

After reconstructing the profile with the process described in Figure 2.3, it is possible to convert the profiles into a series of synthetic indexes which measure roughness severity in a specific wavelength bandwidth. Standard EN 13231-3:2012 [28] presents different requirements and criteria for measurements of the longitudinal and transversal surface

Wavelength range [mm]	Window length [m]
10-30	0.15
30-100	0.5
100-300	1.5
300-1000	5

Table 4.1: Window lengths for the computation of moving average according to [28].

of the rail, as well as reprofiling thresholds. For monitoring purposes, irregularity is measured and compared against defined limits using three possible criteria:

- Moving average of RMS amplitude;
- Moving average of peak-to-peak amplitude;
- Number of irregularities exceeding a specified amplitude.

Among these methods, the criterion using the peak-to-peak amplitude is chosen due to the ease of implementation and the possibility of comparing it to the irregularity data already in possession of *ATM*. The railhead profile $x_{irr,Z}(x)$ is filtered in the wavelength intervals of interest and its moving RMS is computed on a window of spatial length L. The spatial window length and the wavelength intervals are both exposed in Table 4.1. From the RMS it is possible to pass to the peak-to-peak amplitude by multiplying the results for $2\sqrt{2}$.

$$Irr_{Z,Pk-Pk}(n, L) = 2\sqrt{2}\sqrt{\frac{1}{L_n}\int_{x}^{x+L_n} x_{n,Z}(x)\,dx} \tag{4.1}$$

where $x_{n,Z}(x)$ is the irregularity filtered with a zero-phase bandpass filter to the bandwidth of interest and L_n is the window length.

In this thesis, the two wavelength intervals 30-100 mm and 100-300 mm are investigated, due to the presence of corrugation in these two intervals in the Milan subway system.

4.3.2. Results with the different models

It is now possible to compare the moving average of peak-to-peak amplitude profiles estimated starting from the axlebox accelerations, using a single train run. Figure 4.9 contains the resulting peak-to-peak amplitude profiles in the first curve of the section, as well as data coming from measurements of a diagnostic railcar which were taken on the same day. In the wavelength interval of 30-100 mm, the proposed methodology is able to detect corrugation on one side but fails in discerning the side at which corrugation

manifests. They also all overestimate the actual peak-to-peak amplitude. Moreover, the use of different models for wheel-rail interaction produces similar results, confirming the idea that wheelset dynamic plays a minor role at higher frequencies. In fact, at the speed of 30-35 km/h at which the trainset negotiates the curve under analysis, the wavelength interval of 30-100 mm translates into a frequency interval of 90-300 Hz, a region in which the track dynamic starts having larger relevance on the overall response of the system. This is partly less evident in the wavelength range 100-300 mm (corresponding to a frequency interval of 30-90 Hz); here, when the half wheelset model or the full wheelset model with vertical and lateral dynamics are used in the proposed methodology, the estimated profiles show some degree of difference in the irregularities on the two sides. The methodology employing the half wheelset model strongly overestimates corrugation on both sides, while the use of the full wheelset models yields results which are comparable to the profiles measured by a diagnostic draisine. When looking at the 100-300 mm bandwidth on the left side, the use of the full wheelset model with vertical and lateral dynamics reconstructs the profile which more closely matches the measured one. The full wheelset model which accounts for vertical dynamics only, however, shows a strong coupling of the two irregularities in both intervals. Better modeling of the wheelset is able to improve the measurement system output at lower frequencies.

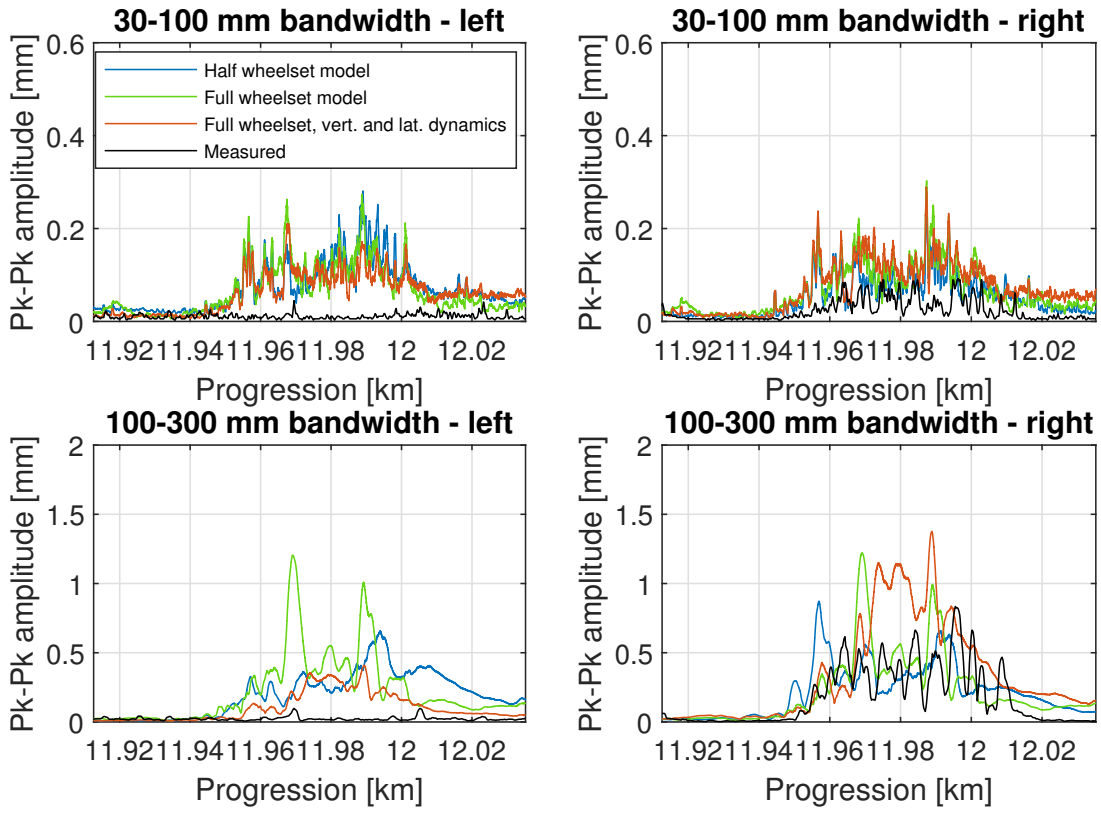

Figure 4.9: Comparison of the three models' results.

4.3.3. Average of multiple runs

In order to improve the accuracy of the results, different runs on the same section can be used to compute an averaged irregularity profile. This is facilitated by the fact that the instrumented trainset runs along the entire line multiple times during each day, thus creating a large dataset. Figure 4.10 presents the moving average of peak-to-peak irregularity profiles of seven runs.

The wavelength range 30-100 mm presents a slightly better roughness reconstruction: despite the algorithm's inability to accurately identify the side at which corrugation appears, a difference between the two sides can be appreciated. The right side shows a more irregular behavior which matches the measured profile, while the profiles on the left side are smoother.

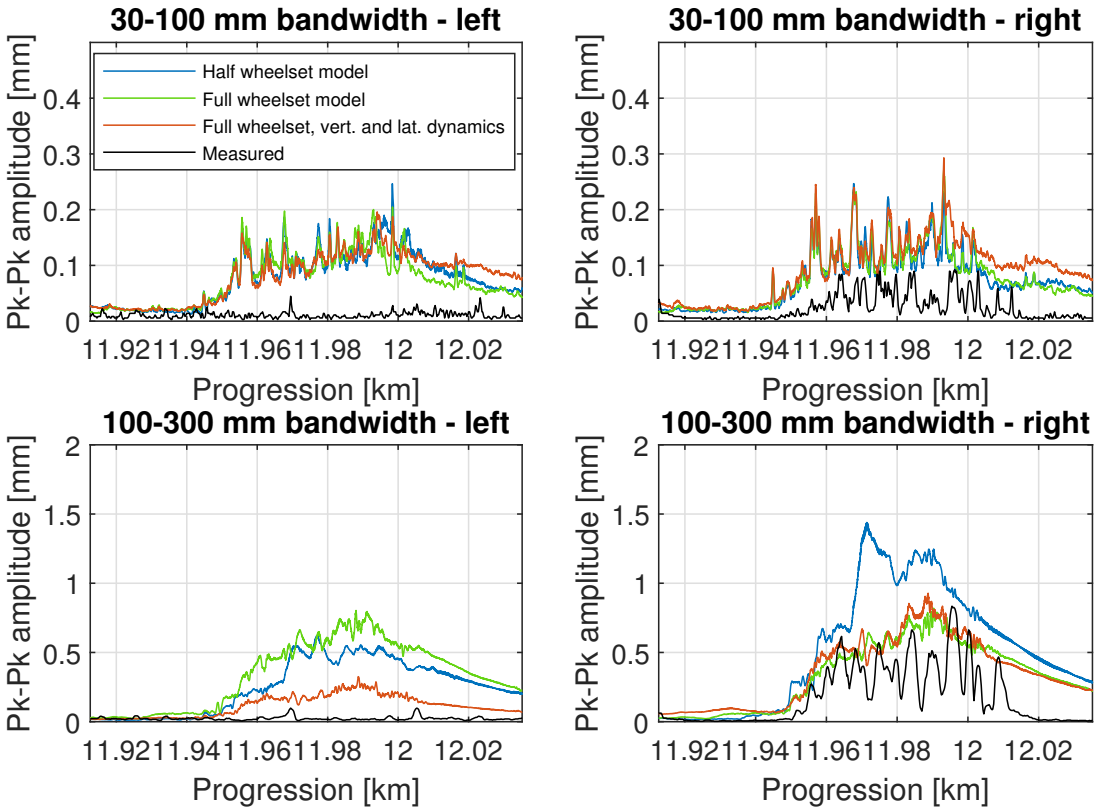

Figure 4.10: Effects of averaging multiple runs.

In the wavelength range of 100-300 mm, the effects of lateral dynamics allow to correctly discern the presence of corrugation on the correct side: moreover, the full wheelset model with both vertical and lateral dynamics is able to outperform all the others in terms of distance from the measured profiles. The half-wheelset model still overestimated the irregularity profiles. The full wheelset model with both vertical and lateral dynamics shows

the overall best performances in reconstructing irregularities in the wavelength range of 100-300 mm, while all the models show similar performances in the range 30-100 mm. Unfortunately, the contact angles needed for implementing lateral dynamics on the full wheelset model are difficult to compute, since additional measuring devices or simulations are needed to compute the contact angles, partially complicating the implementation of this method from a practical point of view.

4.3.4. Influence of uncertainties on wheelset modal parameters

As previously done, the robustness of the algorithm to changes in the measurement conditions is also investigated. In order to do so, a set of 25 modified receptances is used to compute sets of transfer functions and then process the same acceleration time history. Figures 4.11, 4.12 and 4.13 contain the mean roughness value and dotted lines corresponding to a confidence level of 95% of the roughness distribution. The use of the three models showcase a similar level of robustness in the wavelength range 30-100 mm. An analysis over the range 100-300 mm allows to highlight overall better performances for the full wheelset model that accounts for both vertical and lateral dynamics. The half-wheelset model shows the largest confidence interval, suggesting that this model is particularly susceptible to uncertainties in modal parameters. As previously stated, these Figures underline how small changes in the modal parameters or in the measurement conditions can cause large variations in the final results. This undermines the reliability of rail profiles reconstructed from acceleration measurements since even relatively small speed variations or differences in wheel wear can cause large differences in the reconstructed profiles. The Automatic Train Operator and Control system featured in the rolling stock of the underground line *M1* is able only to partially alleviate this issue, while the averaging of different reconstructed profiles improves the robustness of the overall results.

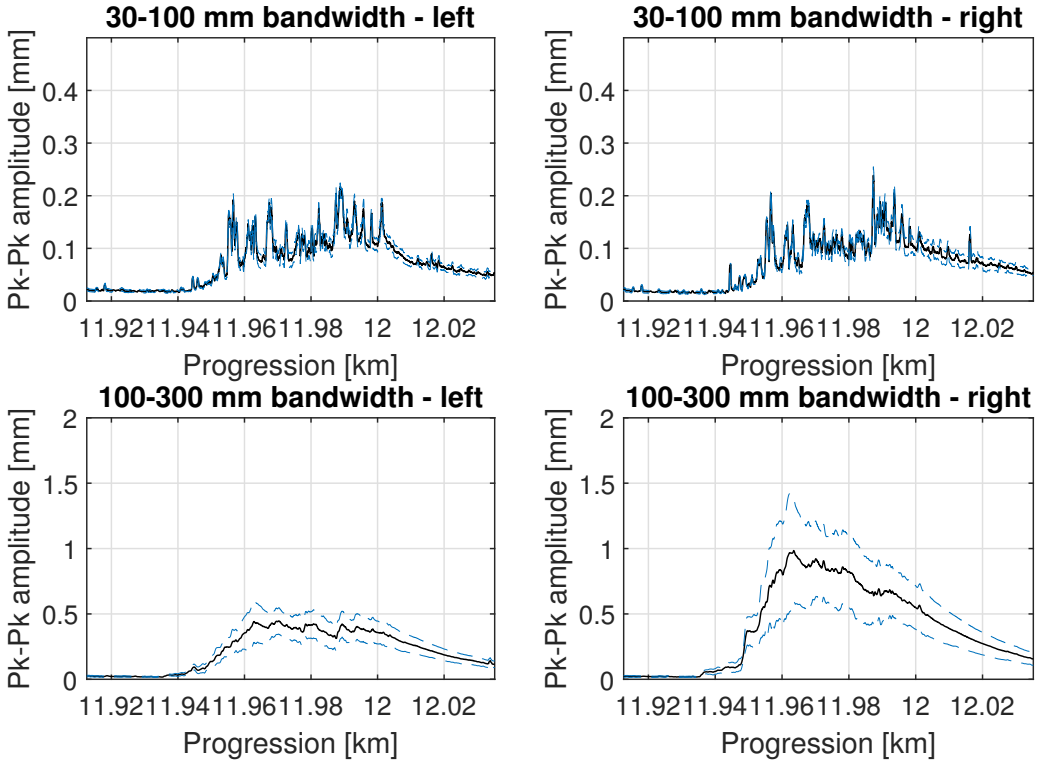

Figure 4.11: Confidence intervals: half wheelset model.

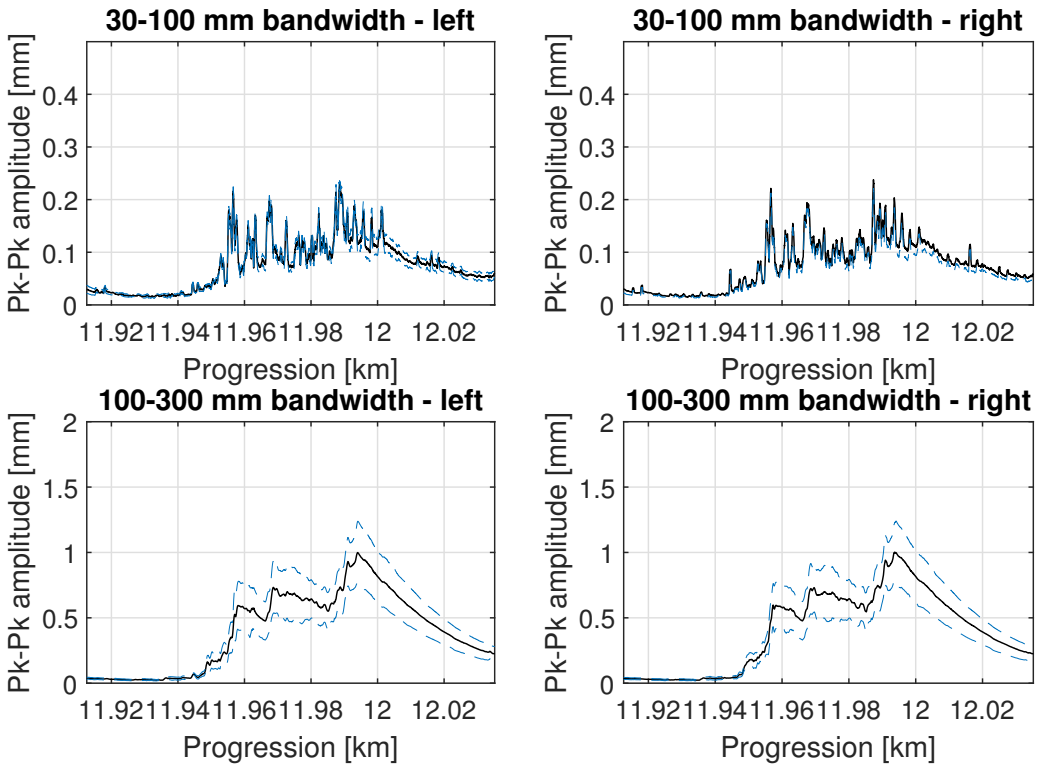

Figure 4.12: Confidence intervals: full wheelset model.

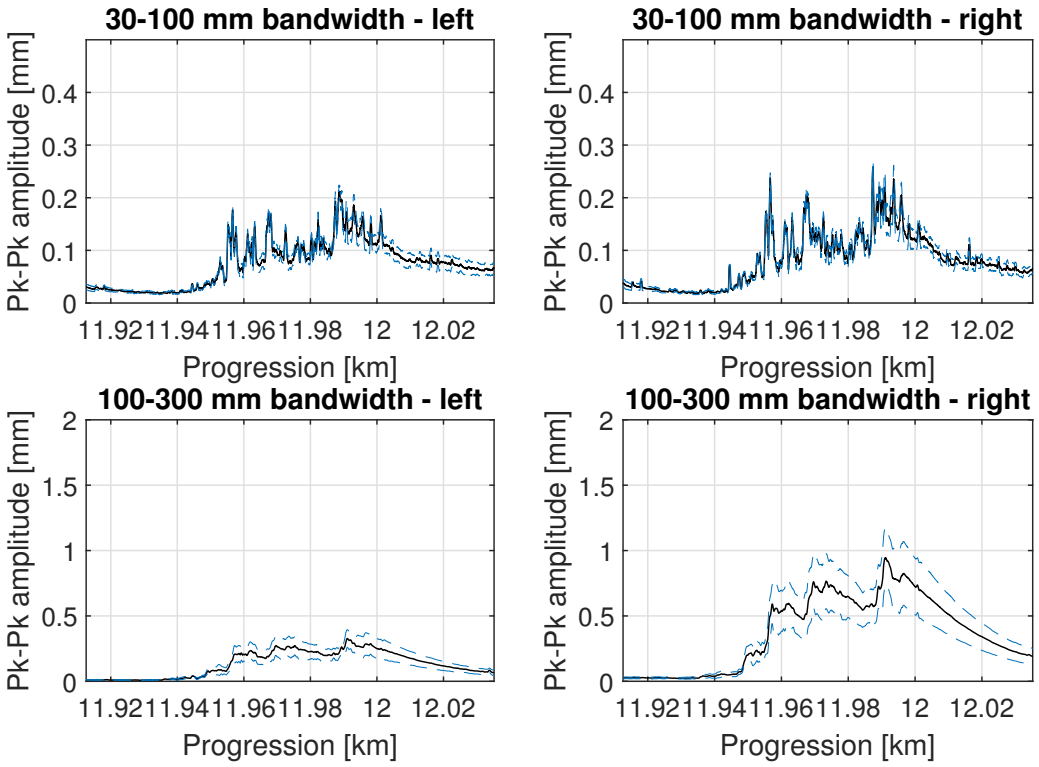

Figure 4.13: Confidence intervals: full wheelset model with vertical and lateral dynamics.

4.3.5. Influence of accelerometers positioning

The influence of the placement of the accelerometers on the axleboxes is then investigated. During the simulations, the receptances of the accelerometer placement points were computed under the hypothesis that they were positioned in the axleboxes' center. However, the experimental setup is seldom precisely centered, due to the physical impossibility of placing the accelerometer exactly in the desired location, tolerances, or minor misalignments in the wheelset. Therefore, a new set of receptances is computed, imposing a shift in the accelerometers of ± 10 mm, ± 30 mm and ± 50 mm from the nominal position. These receptances are used to compute a set of transfer functions which are in turn used to analyze a line section. Figure 4.14 highlights the various roughness profiles identified using different transfer functions. It is possible to notice how even small errors in the placement of the accelerometer may result in large differences when reconstructing the roughness profiles. Particular care must therefore be taken in the vehicles' setup in order to have reliable and comparable data.

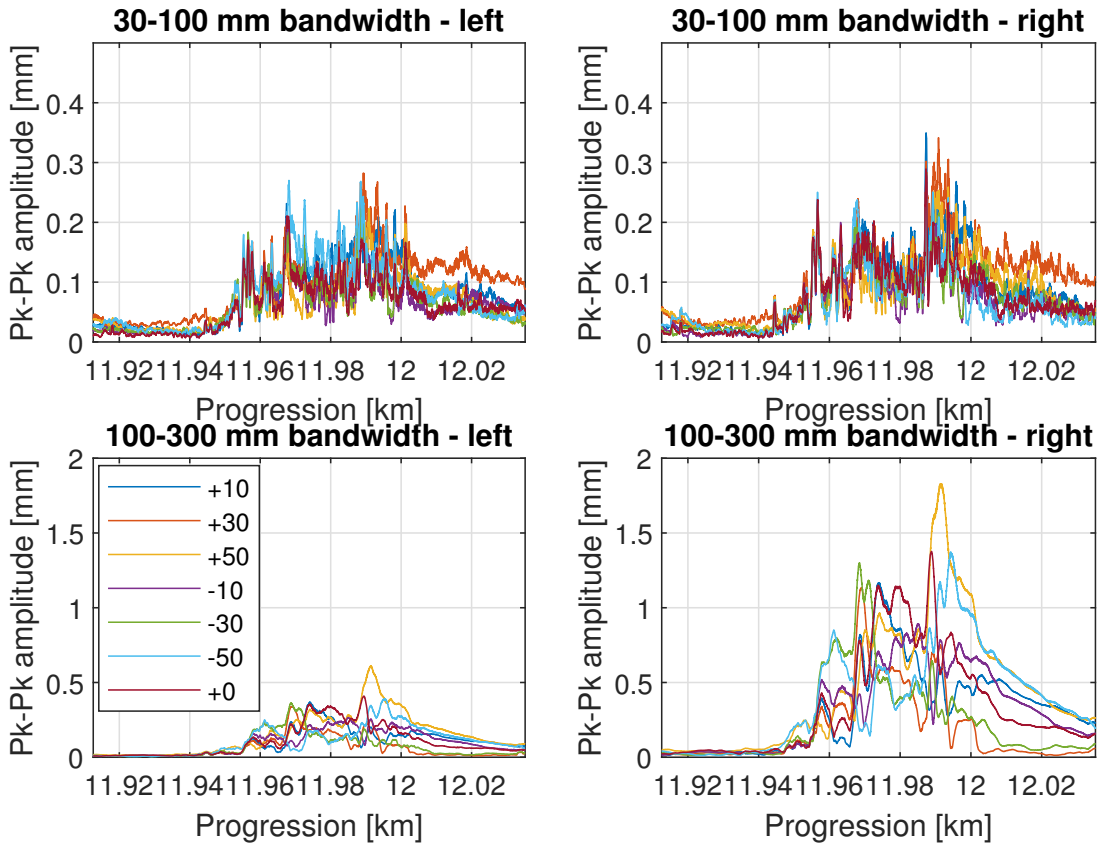

Figure 4.14: Effects of accelerometers placement: detailed view.

Figure 4.15 showcases the mean value the 95% confidence intervals of the roughness profiles with different placement of the accelerometers depicted in Figure 4.14. The large dispersion of the results confirms that differences in the correct palcement of the accelerometers can have large impacts on the final outcome of the algorithm.

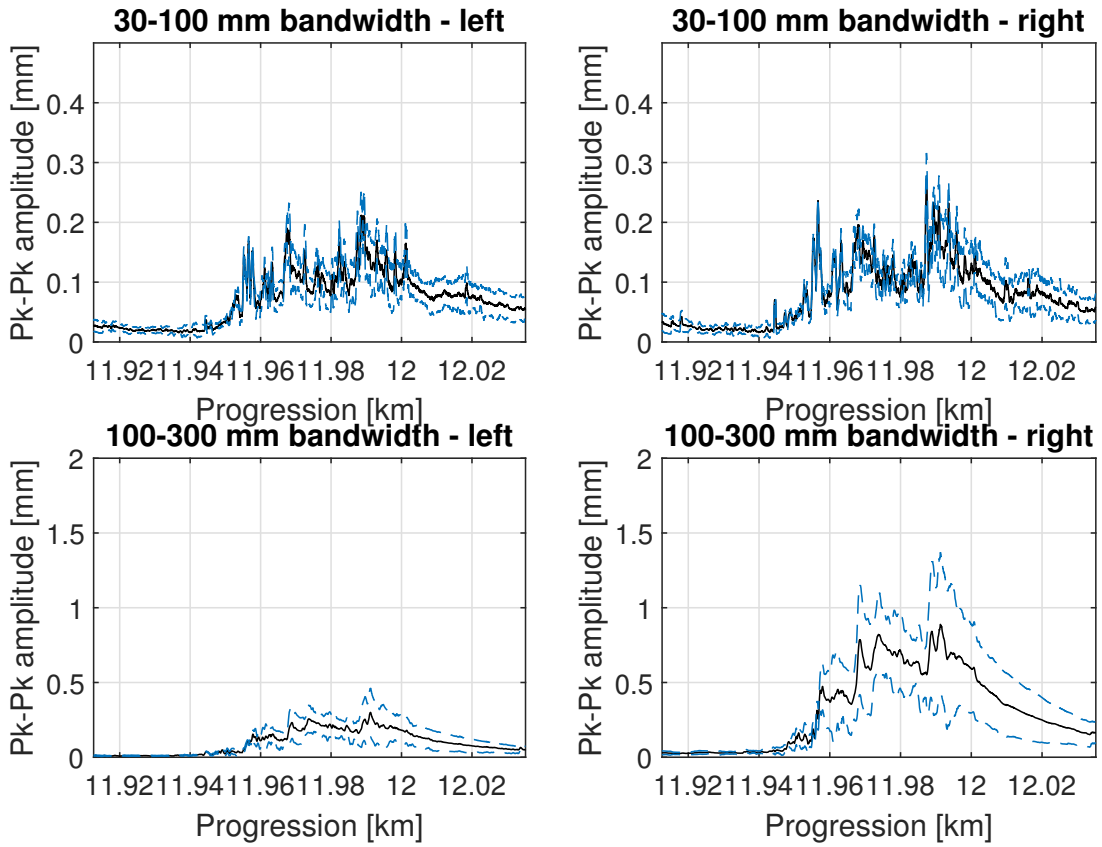

Figure 4.15: Effects of accelerometers placement: confidence intervals.

4.3.6. Monitoring of rail corrugation evolution

Finally, the possibility of tracking the evolution of corrugation of the rail profile is investigated. In order to do so, a set of days are selected to cover the period between two consecutive grinding operation over the span of three months. For each day under analysis, all the runs recorded by the instrumented trainset are averaged in order to improve their robustness. All data are processed using the full wheelset model and accounting for both vertical and lateral dynamics. The results for each day are plotted in Figure 4.16. For reference, the measurements taken the day after grinding are averaged and plotted with a dotted line. Figure 4.16 underlines how the obtained roughness profiles are able to track the development of corrugation over time. The numerous acceleration measurements taken each day allow to mediate them, improving robustness, while the continuous coverage of the section under analysis over time permits the monitoring of corrugation and other defects over time. Moreover, a large decrement in roughness after the grinding operation is shown, suggesting the successful removal of rail irregularities. Therefore, acceleration measurements could be used as a follow-up practice to trace the correct removal of irregularity after rail grinding.

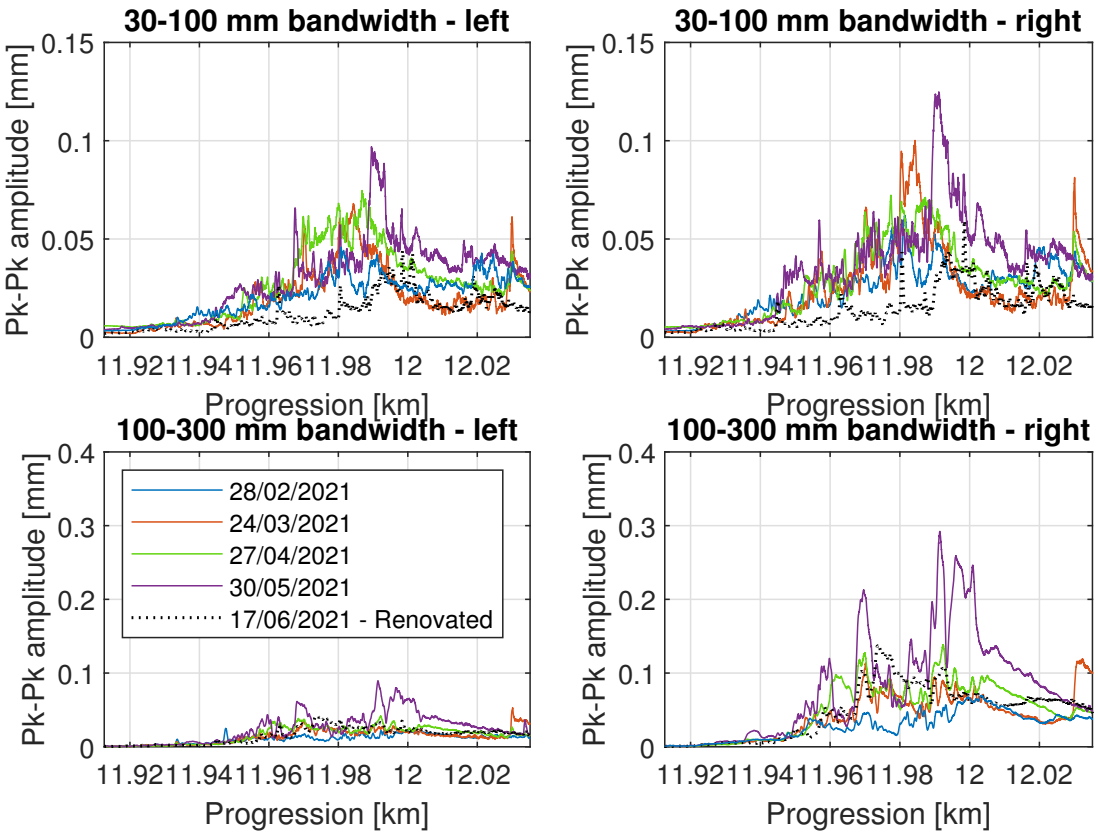

Figure 4.16: Roughness evolution over time.

5 | Conclusions and future developments

The objective of this thesis is the development of an algorithm for the identification and monitoring of rail corrugation growth by interpreting acceleration data coming from an instrumented trainset. Different models of wheel-rail interaction allow for the computation of the measurement system transfer function, which is used to process acceleration data and estimate the irregularity profiles. Information on the evolution of rail corrugation can therefore be used to relay data regarding the line sections to prioritize for maintenance operation. The monitoring activity is performed in a specific section of Milan's underground network, characterized by the trackform *Milano Modificato*: such a trackform is widely used in Milan's subway network. The instrumented vehicle is a *Meneghino* trainset, which passes over the side under analysis multiple times per day. One of the unpowered bogies of the trainset is equipped with a set of accelerometers measuring vertical acceleration of the axleboxes.

The aforementioned models are derived by taking three different approaches for modeling the wheel-rail interaction. The first one is based on a state-of-the-art model of a flexible half-wheelset which neglects the coupling between the two wheels, as previously done in literature. Wheel-rail interaction is assumed to be aligned to the vertical direction. The second approach introduces the full dynamic of the wheelset and therefore the coupling between the two sides, creating a multi-input, multi-output model. Forces and displacements are still considered to act in the vertical direction only. The effect of the inclination of the wheel-rail contact planes is subsequently added to the third and last model, thereby introducing the effect of the lateral dynamics of the full wheelset. The wheelset is modeled by means of a modal model whose mode shapes have been obtained through a Finite Element simulation and whose eigenfrequencies are adjusted according to the results of an experimental modal identification campaign. The rail behavior is modeled as an infinite, continuously supported Timoshenko beam.

The models of the wheel-rail interaction are used to compute the transfer functions be-

tween rail irregularity and axlebox acceleration. The irregularity profiles are reconstructed starting from the spectra of the axlebox acceleration time histories which are measured by the instrumented trainset. The acceleration spectra are multiplied for the transfer functions of the measurement system and the resulting irregularity spectra are transformed back to the time domain by means of an inverse Fourier transform. Literature suggests that axlebox acceleration measurement systems cannot reliably and precisely estimate the whole rail profile. It is however seldom necessary to reconstruct it entirely: Standard EN 13231-3:2012 explains how to synthetically report irregularity by filtering the obtained rail profiles according to a series of bandwidths defined by the standard and computing the moving average of peak-to-peak irregularity amplitude in each wavelength interval. This allows for a convenient expression of irregularity profiles in the space domain.

Acceleration data coming from the instrumented trainset is then used to reconstruct the irregularity profile of a section of the Milan subway by means of an algorithm employing the three aforementioned models. Their results are compared against irregularity data coming from a diagnostic draisine and acquired on the same day. The section under analysis is characterized by two curves, with corrugation appearing in the lower rail of both. This thesis focuses on the first right curve. A multibody simulation of the train negotiating the curve is performed in order to obtain the inclination of the two wheel-rail contact planes.

The proposed methodology is unable to discern the side at which corrugation manifests in the wavelength band of 30-100 mm. However, an analysis of the response in the wavelength band of 100-300 mm shows that, when the algorithm employs the full-wheelset model with the effects of both vertical and lateral dynamics for the computation of the measurement system transfer function, it is able to correctly discern the side at which corrugation appears. The full-wheelset model with only the contribution of vertical dynamics shows unsatisfactory performances since the model's dynamic creates a coupling between the acceleration measured on one side and the two reconstructed irregularities. The use of the half wheelset model results in a correct identification of the side at which corrugation appears but errors in its amplitude.

More robust results can be improved by averaging the results of multiple runs. This is facilitated by the fact that the instrumented trainset is able to travel along the test section multiple times per day. Averaging several runs over a single day improves the results for all models.

The influence of uncertainties in the modeling of wheel-rail dynamic and variations of the measurement conditions is investigated. It is found that small variations in the compu-

tation of the transfer function of the measurement system or changes in the condition in which measurements are taken (speed, wear in wheels and rail, etc...) can severely impact the final results. The robustness of the measurement system is also investigated in the frequency domain: results highlight that the measurement system shows the largest result dispersion in correspondence to excitation which matches the resonance frequencies of the wheel-rail dynamic. This has a huge impact on the reliability of the results, since the corrugation spatial wavelengths are usually associated to the natural frequencies of the system.

The evolution of corrugation over time is finally investigated by analyzing acceleration acquisitions taken over a period of three months and processing them with the full wheelset model with both vertical and lateral dynamics. The measurement system is correctly able to trace the evolution of corrugation over time and the effects of a rail grinding operation performed at the end of the analysis period.

A possible development of this thesis could be the analysis of acceleration data measured at speeds different from the usual line speed imposed by the *Automatic Train Operator* system, in order to validate the possibility of using axlebox acceleration measurements to correctly and reliably reconstruct the irregularity profiles. Alternatively, the possibility of removing the effects of speed variation in the estimation of irregularity profiles could be investigated.

Bibliography

[1] S. Ricci. *Ingegneria dei sistemi ferroviari*. EGAF, 2013.

[2] H. Tsunashima, A. Matsumoto, T. Mizuma, H. Mori, and Y. Naganuma. *Condition Monitoring of Railway Track Using In-Service Vehicle*, volume 3. 03 2012. ISBN 978-953-51-0451-3. doi: 10.1299/jmtl.3.154.

[3] S. Li, A. Núñez, Z. Li, and R. Dollevoet. Automatic detection of corrugation: Preliminary results in the dutch network using axle box acceleration measurements. *Joint Rail Conference*, 2015. doi: 10.1115/JRC2015-5730.

[4] P. Weston, C. Roberts, G. Yeo, and E. Stewart. Perspectives on railway track geometry condition monitoring from in-service railway vehicles. *Vehicle System Dynamics*, 53(7):1063–1091, 2015. doi: 10.1080/00423114.2015.1034730.

[5] E. Fumeo, L. Oneto, and D. Anguita. Condition based maintenance in railway transportation systems based on big data streaming analysis. *Procedia Computer Science*, 53, 2015. ISSN 18770509. doi: 10.1016/j.procs.2015.07.321.

[6] S. L. Grassie and J. Kalousek. Rail corrugation: characteristics, causes and treatments. *Proceedings of the Institution of Mechanical Engineers, Part F: Journal of Rail and Rapid Transit*, 207(1):57–68, 1993.

[7] M. Bocciolone, A. Caprioli, A. Cigada, and A. Collina. A measurement system for quick rail inspection and effective track maintenance strategy. *Mechanical Systems and Signal Processing*, 21, 2007. ISSN 08883270. doi: 10.1016/j.ymssp.2006.02.007.

[8] S. L. Grassie. Measurement of railhead longitudinal profiles: A comparison of different techniques. *Wear*, 191, 1996. ISSN 00431648. doi: 10.1016/0043-1648(95)06732-9.

[9] S. L. Grassie. A practical methodology to prioritise reprofiling sites for corrugation removal. *Proceedings of the Institution of Mechanical Engineers, Part F: Journal of Rail and Rapid Transit*, 234, 2020. ISSN 20413017. doi: 10.1177/0954409719853071.

[10] J. Karaki, L. Faccini, E. Di Gialleonardo, C. Somaschini, M. Bocciolone, and A. Collina. Continuous monitoring of rail corrugation growth using an in-service vehi-

cle. In Anna Orlova and David Cole, editors, *Advances in Dynamics of Vehicles on Roads and Tracks II*, pages 158–167. Springer International Publishing, 2022. doi: 10.1007/978-3-031-07305-2_17.

[11] L. Faccini, J. Karaki, E. Di Gialleonardo, C. Somaschini, M. Bocciolone, and A. Collina. A methodology for continuous monitoring of rail corrugation on subway lines based on axlebox acceleration measurements. *Applied Sciences*, 13(6), 2023. ISSN 2076-3417. doi: 10.3390/app13063773.

[12] S. L. Grassie. Rail corrugation: Characteristics, causes, and treatments. *Proceedings of the Institution of Mechanical Engineers, Part F: Journal of Rail and Rapid Transit*, 223, 2009. ISSN 09544097. doi: 10.1243/09544097JRRT264.

[13] F. Mauz, R. Wigger, T. Wahl, M. Kuffa, and K. Wegener. Acoustic roughness measurement of railway tracks: Implementation of a chord-based optical measurement system on a train. *Applied Sciences*, 12:11988, 11 2022. doi: 10.3390/app122311988.

[14] E. Tassilly and N. Vincent. A linear model for the corrugation of rails. *Journal of Sound and Vibration*, 150(1):25–45, 1991. ISSN 0022-460X. doi: https://doi.org/10.1016/0022-460X(91)90400-E.

[15] S. L. Grassie. Measurement of longitudinal irregularities on rails using an axlebox accelerometer system. pages 320–328, 2021. doi: 10.1007/978-3-030-70289-2_33.

[16] Qinglin Xie, Gongquan Tao, Bin He, and Zefeng Wen. Rail corrugation detection using one-dimensional convolution neural network and data-driven method. *Measurement*, 200:111624, 2022. ISSN 0263-2241. doi: https://doi.org/10.1016/j.measurement.2022.111624.

[17] J.C.O. Nielsen. Numerical prediction of rail roughness growth on tangent railway tracks. *Journal of Sound and Vibration*, 267(3):537–548, 2003. ISSN 0022-460X. doi: https://doi.org/10.1016/S0022-460X(03)00713-2. Proceedings of the Seventh International Workshop on Railway Noise.

[18] J.C.O. Nielsen and A. Igeland. Vertical dynamic interaction between train and track influence of wheel and track imperfections. *Journal of Sound and Vibration*, 187(5):825–839, 1995. ISSN 0022-460X. doi: https://doi.org/10.1006/jsvi.1995.0566.

[19] A. Pieringer and W. Kropp. Model-based estimation of rail roughness from axle box acceleration. *Applied Acoustics*, 193:108760, 2022. ISSN 0003-682X. doi: https://doi.org/10.1016/j.apacoust.2022.108760.

[20] G. Diana, F. Cheli, S. Bruni, and A. Collina. Experimental and numerical investiga-

tion on subway short pitch corrugation. *Vehicle System Dynamics*, 29(sup1):234–245, 1998. doi: 10.1080/00423119808969562.

[21] C. O. Frederick. A rail corrugation theory. *Proc. Int Symp. on Contact Mechanics and Wear of Rail/Wheel Systems II*, 1986.

[22] T. D. Carrigan and J. P. Talbot. Use of flexible wheelset model, comb filter and track identification to derive rail roughness from axle-box acceleration in the presence of wheel roughness. In *Proceedings of 14th International Workshop On Railway Noise*, pages 232–239. INTEX, 2022.

[23] K. Knothe and S. Stichel. *Rail Vehicle Dynamics*. Springer, 2003.

[24] F. Cheli and G. Diana. *Advanced Dynamics of Mechanical Systems*. Springer, 2015.

[25] BS EN 13674-1:2011. standard, BSI Group.

[26] D. Thompson. *Railway Noise and Vibration*. Elsevir, 2009.

[27] M. Tarabini. *Experimental Characterization of Mechanical Systems*. CEMB, 2020.

[28] BS EN 13231-3:2012. standard, BSI Standard Publications.

List of Figures

List of Tables